

A comprehensive analysis toward the Fermi-LAT source 4FGL J1846.9–0227

Jets of a proto-planetary nebula producing γ -rays?

MARTÍN E. ORTEGA,¹ ALBERTO PETRIELLA,¹ AND SERGIO PARON¹

¹CONICET-Universidad de Buenos Aires. Instituto de Astronomía y Física del Espacio, Ciudad Universitaria, (C1428EGA) Ciudad Autónoma de Buenos Aires, Argentina

ABSTRACT

Most of the gamma-ray sources in the Fermi-LAT 14-year Source Catalog are associated with pulsars and blazars. However, unveiling the nature of the still unassociated gamma-ray sources is important for the understanding of high energy emission mechanisms in astrophysical objects. This work presents a comprehensive study toward the region covered by the Fermi source 4FGL J1846.9–0227 previously suggested to be a blazar or a massive protostar. Using multiwavelength observations, we analyzed several astrophysical objects in the region as possible counterparts of the Fermi-LAT source. Having discarded most of them after a comprehensive analysis, we suggest that the most likely candidate to be such a counterpart is IRAS 18443–0231. We discovered that this source, previously cataloged as a planetary nebula candidate, actually is a proto-planetary nebula. The radio continuum image at 3 GHz associated with such a nebula allowed us to identify a jet-like structure. Additionally, we identified an associated red-shifted CO molecular outflow and a dense molecular clump in which the source is embedded. We obtained a radio spectral index of -0.47 ± 0.08 for the source, indicating synchrotron emission due to accelerated particles. Thus, we suggest that processes such as proton-proton collisions and relativistic Bremsstrahlung are likely to occur. IRAS 18443–0231, lying almost at the center of the Fermi confidence ellipse and related to the hard X-ray source 4XMM J184700.4–022752, would be the first association between a proto-planetary nebula and gamma emission.

Keywords: Gamma rays: ISM – (Stars:) binaries: symbiotic – (ISM:) planetary nebulae: general

1. INTRODUCTION

Fermi-LAT unassociated sources represent some of the most enigmatic gamma-ray sources in the sky. In the latest data release from the Fermi Gamma-ray Space Telescope (the 4th Fermi LAT 14 yr Catalog, or 4FGL-DR4), containing 7194 gamma-ray sources (Ballet et al. 2023), more than 50% of the suspected Galactic sources (i.e., $|b| \leq 5^\circ$) are yet to be identified (Rangelov et al. 2024).

The nature of the gamma-ray sources may be varied, they can be pulsar-wind nebulae (PWNe) and supernova remnants (SNRs) (e.g. Acero et al. 2013 and Cao et al. 2023), active galactic nuclei (AGNs; e.g. Madejski & Sikora 2016), massive young stellar objects (MYSOs; e.g. de Oña Wilhelmi et al. 2023), X-ray binaries (XRBs; e.g. Kretschmar et al. 2019 and Bahramian & Degenaar 2023), and

classic- and symbiotic-novae (Franckowiak et al. 2018). According to the 4FGL catalogs, many of the GeV-emitting PWNe and SNRs are found to be extended LAT sources, many AGNs are found to be variable sources, classical and symbiotic novae are only found to be GeV emitters during outbursts, and MYSOs were argued to be GeV emitters based mainly on positional coincidences.

In short, any source capable of accelerating particles should be considered as a possible responsible of the gamma-ray emission. Thus, given the great variety of objects that can emit at high energies and given the typical spatial extent of the Fermi sources, revealing the nature of unidentified gamma-ray sources requires comprehensive multiwavelength studies both of the possible objects and their associated emission mechanisms.

4FGL J1846.9–0227 gamma-ray source (first cataloged as 1FGL J1846.8-0233c) was proposed to be associated with the MYSO candidate MSX6C G030.1981–00.1691 (hereafter MSX G30; Munar-Adrover et al. 2011), based on the spatial correlation between both sources and considering the absence, according to the knowledge at that time, of other possible counterparts. Massive protostars have associated energetic jets and molecular outflows that can produce strong shocks during the interaction with the ambient gas. At these shocks, particles can be accelerated up to relativistic energies producing gamma-ray emission, as some theoretical models predict (e.g., Araudo & Rodríguez 2012; Bosch-Ramon et al. 2010).

A decade later, Kerby et al. (2021) analyzed a sample of 174 unknown Fermi sources with a single X-ray/UV/optical counterpart. The authors developed a method to discern between pulsars and blazars, given that the most of the sources of 4FGL catalog are these types of objects. In particular, the authors found two Swift-XRT X-ray sources as possible counterpart of the gamma-ray source 4FGL J1846.9–0227. The first one, SwXF4 J184650.7–022904, was rejected as possible pulsar or blazar because of its extreme photon index in the X-ray band ($\Gamma_X \sim 7.9$). Moreover, the authors warned about the positional coincidence (shifted about 4'') of this Swift-XRT source with a dim star, suggesting that the high ‘blazar probability value’ obtained should not be trusted, given that UV/optical emission would not be related to the blazar. On the other hand, the second Swift source identified towards the region, SwXF4 J184651.6–022507, whose X-ray flux is three orders of magnitude smaller than the first one, was characterized as a likely blazar.

It is worth mentioning that despite all the studies carried out to date, the exact origin of the γ -ray emission from 4FGL J1846.9–0227 remains unknown. In fact, in the last two incremental versions (4FGL-DR3 and 4FGL-DR4) of the fourth Fermi Large Area Telescope (LAT) catalog of γ -ray sources (Abdollahi et al. 2022 and Ballet et al. 2023, respectively), this source still appears as ‘unknown’. However, it is important to mention that both catalogs refer to a possible association with the radio source TXS 1844–025 mentioned in Honma et al. (2000). Using the Japanese VLBI Network, the authors carried out radio continuum observations at 22 GHz toward a sample of 267 radio sources selected from existing radio surveys. In particular, they did not detect emission at 22 GHz towards the source TXS 1844–025. This radio source is in positional coincidence with the infrared source IRAS 18443–0231, which is cataloged as a planetary nebula (PN) candidate (Yang et al. 2016; Irabor et al. 2018, and references therein).

Summarizing, since the nature of 4FGL J1846.9–0227 is still unknown, we present a comprehensive and multi-wavelength analysis of all candidate sources in the region to identify definitely the origin of the γ -ray emission. It is important to highlight that this type of in-depth studies of specific sources are necessary to complement the statistical studies.

2. DATA

The study of the origin of the γ -ray emission of 4FGL J1846.9–0227 involved the analysis of a multiwavelength set of data. In what follows, we describe each dataset.

2.1. *Radio continuum data*

We used centimeter radio continuum data from several surveys:

- The continuum at 20 cm (\sim 1.4 GHz) was extracted from the Multi-Array Galactic Plane Imaging Survey (MAGPI; [Helfand et al. 2006](#)), which has an angular resolution and sensitivity of about $5''$ and 2 mJy beam $^{-1}$, respectively. Even with data from the D configuration, the resulting maps suffer missing flux from large-scale structure (above $1'$) to which the VLA is insensitive. To correct for this deficiency, the VLA images were combined with images from a 1400 MHz survey made with the Effelsberg 100 m telescope ([Reich et al. 1990](#), beam $\sim 9.4''$).
- The continuum between between 4 and 8 GHz was extracted from GLOSTAR Galactic plane survey ([Brunthaler et al. 2021](#)), which uses the Very Large Array (VLA) with the D-array configuration. We retrieved the image averaged over the full bandwidth from the Image Server¹, which has a representative frequency of 5.8 GHz and are convolved with a $18'' \times 18''$ (FWHM) Gaussian kernel. It is worth noting that these observations also are affected by the missing flux problem inherent to interferometric observations. For sources of a few arcmin, the non-recovered flux can be as large as 90% (see Figure 4 of [Dokara et al. 2021](#)).
- We also used data from the THOR Survey². This survey has mapped the Galactic plane between 1 and 2 GHz using the C-array configuration of the VLA at a native resolution of (FWHM) $\sim 12'' \times 14''$.
- The radio continuum at 3 GHz was extracted from the VLA Sky Survey (VLASS; [Lacy et al. 2020](#)). This survey covers the whole sky visible to the VLA (decl. ≥ -40 deg). The angular resolution and sensitivity are about $2.5''$ and 100 μ Jy beam $^{-1}$, respectively. The largest angular scale is about $30''$.
- The radio continuum at 5 GHz was extracted from the Co-Ordinated Radio 'N' Infrared Survey for High-mass star formation (CORNISH; [Purcell et al. 2008](#)). The survey was conducted using the Karl Jansky Very Large Array in B-configuration, yielding a $1.5''$ resolution map with a noise level ≤ 0.4 mJy/beam $^{-1}$. The largest angular scale is $15''$.

2.2. *Mid-infrared and submillimeter data*

- Mid-infrared data from the IRAC-Spitzer and MIPS-Spitzer at 8 and 24 μ m were obtained from the GLIMPSE survey ([Churchwell et al. 2009](#)) and from the MIPSGAL survey ([Carey et al. 2005](#)), respectively. IRAC images have an angular resolution of about $1.7''$ and the MIPSGAL angular resolution is $6''$ at 24 μ m.
- Submillimeter data at 850 μ m with a beam size of $13.5''$ obtained from the Submillimetre Common-User Bolometer Array (SCUBA; [Di Francesco 2008](#)) using the James Clerk Maxwell Telescope.

¹ Available at https://glostar.mpifr-bonn.mpg.de/glostar/image_server.

² <https://www2.mpi-a-hd.mpg.de/thor/Overview.html>

- The ^{12}CO J=3–2 data from the James Clerk Maxwell Telescope (JCMT) was extracted from the Canadian Astronomy Data Centre. The PI and proposal ID are Lumsden, S. and M07AU08, respectively. The angular and velocity resolutions are $15''$ and 0.4 km s^{-1} , respectively. The rms noise level is about 0.1 K.

2.3. ALMA data

The data cube from the project 2015.1.01312 (PI: Fuller, G.; Band 6) were obtained from the ALMA Science Archive³. The single pointing observation for the target was carried out using the telescope configurations with L5BL/L80BL(m) 42/222 in the 12 m array. The frequency range used in our analysis goes from 224.3 to 226.3 GHz. The angular resolution is $0''.7$. The maximum recoverable scale is about $6''.2$. The field of view is $25''$. The frequency and velocity resolutions are 1.1 MHz and 1.4 km s^{-1} , respectively. The continuum and line (10 km s^{-1} averaged) sensitivity are 0.2 and 1.5 mJy beam $^{-1}$, respectively.

Although the data of the project passed the QA2 quality level, which assures a reliable calibration for ‘science ready’ data, we reprocessed the raw data using CASA 4.5.1 and 4.7.2 versions and the calibration pipeline scripts to check the final images. Particular care was taken with the different parameters of *clean* the task. The images and spectra obtained from our data reprocessing —after several runs of the *clean* task, varying some of its parameters— were very similar to those obtained from the archival data. Briefly, the quality of the images automatically processed by the ALMA team could not be improved.

The task *imcontsub* in CASA was used to subtract the continuum from the spectral lines using a first-order polynomial. To that frequency ranges without molecular line emission were carefully selected. The continuum map at 240 GHz was corrected for primary beam. Several continuum subtraction tests were performed to ensure a reliable 240 GHz continuum map, which involved the selection of different free line regions of the spectrum. It is important to note that the beam size of the 240 GHz continuum data in the 12 m array provides a spatial resolution of about 0.02 pc (~ 4000 au) at 5.4 kpc, which is the kinematic distance assigned to the MYSO candidate MSX G030.

2.4. XMM-Newton data

The positional error ellipse of 4FGL J1846.9–0227 falls within the field-of-view of the XMM-Newton observations 0651680301 and 0823990801, hereafter Obs1 and Obs2, respectively. The observations were pointed to the supergiant fast-X-ray transient IGR J18462–0223, and the centroid of the Fermi source is located $\sim 12'$ off-set from the center of the X-ray cameras. The duration of Obs1 and Obs2 are 33.4 and 35.7 ks, respectively. We used the Science Analysis System (SAS, version 21.0.0) and HEASoft (version 6.33.2) for data reduction and spectral analysis. We applied the standard procedure to obtain a calibrated event file for each observation using the updated set of calibration files (CCF). We use these event files to produce light curves in the high-energy domain (> 10 keV) and filtered out periods of high-count rate associated with background flares. We applied additional filtering to include events with FLAG = 0 and PATTERN ≤ 12 and 4 for PN and MOS cameras, respectively. In Table 1 we report a summary of the X-ray observations.

3. RESULTS

³ <http://almascience.eso.org/aq/>

Table 1. Summary of the XMM-Newton observations. The *Net exposure* column reports the effective exposure time after filtering the periods of high-count rate.

Obs. ID (date)	Camera	Science mode	Net exposure (ks)
0651680301 (Apr. 18, 2011)	MOS1	Full Frame	30.8
	MOS2	Full Frame	31.6
	PN	Full Frame	15.1
0823390801 (Oct. 22, 2018)	MOS1	Small Window	31.3
	MOS2	Timing	31.1
	PN	Full Frame	14.5

Fermi-LAT sources typically have positional errors of a few arcminutes, which implies that there are often several candidates to be the counterpart of the high energy source. Figure 1 shows a three color image with 8 and 24 μm , and 20 cm emissions represented in green, red, and blue, respectively. The center and the 95% confidence ellipse of the Fermi source 4FGL J1846.9–0227 are represented by the yellow cross and the dashed-yellow ellipse, respectively. We carried out the search for the Fermi counterpart in the region within such an ellipse.

Figure 2-left panel shows the whole field of view of the XMM-Newton observations with the X-ray energy band between 0.5 keV and 8.0 keV. This image was obtained by combining the 6 images and exposure maps of the mos1, mos2 and pn cameras of each observation using the *emosaic* task of SAS. We applied a Gaussian smoothing to increase the S/N ratio. Figure 2-right panel shows a two-color image of the X-ray soft/medium and hard emissions between 0.5 and 2.0 keV (red) and 2.0 and 8.0 keV (green), respectively. No hint of diffuse emission coincident with the Fermi source and some point sources can be clearly observed. The brightest X-ray point source, by far, coincident with the Fermi positional error ellipse is 4XMM J184650.6–022907 (associated with SwXF4 J184650.7–022904), a soft source with no counts detected above 3.0 keV. Additionally are indicated the soft X-ray source 4XMM J184651.2–022504 (associated with SwXF4 J184651.6–022507) and the hard X-ray source 4XMM J184700.4–022752 (associated with the PN candidate IRAS 18443–0231). These sources are analyzed below.

The region considered for the analysis includes four centimeter radio continuum sources (see Fig. 1 and Fig. 3-left). G030.213–00.156 (hereafter G30.21) is cataloged as an HII region with a radio recombination line at 100 km s^{-1} , which corresponds to the near kinematic distance of about 5.4 kpc (Anderson et al. 2015). Southwards G30.21, we identify an uncatalogued extended radio continuum source. It is worth noting that both radio sources, which seem not to be connected, exhibit an evident flattening facing a conspicuous dust filament seen at 8 and 24 μm (see Fig. 1 and Fig. 3-left). It is possible that both radio sources compress such a dust filament generating its flattened morphology. It is important to mention that Anderson et al. (2015) used Green Bank Telescope radio observations, whose angular resolution of about 87" prevented them from resolving both radio sources, which were considered as a single one.

Interestingly, the peak of emission of the HII region G30.21 is in positional coincidence with an illuminated protrusion of the filament, while the peak of emission of the new radio continuum source appears located close to the MYSO candidate MSX G30, which seems to be surrounded by diffuse and extended gas (see Fig. 3-left). Anderson & Bania (2009) determined a kinematic distance of about 5 kpc for MSX G30. The morphological coincidence between the uncatalogued radio continuum

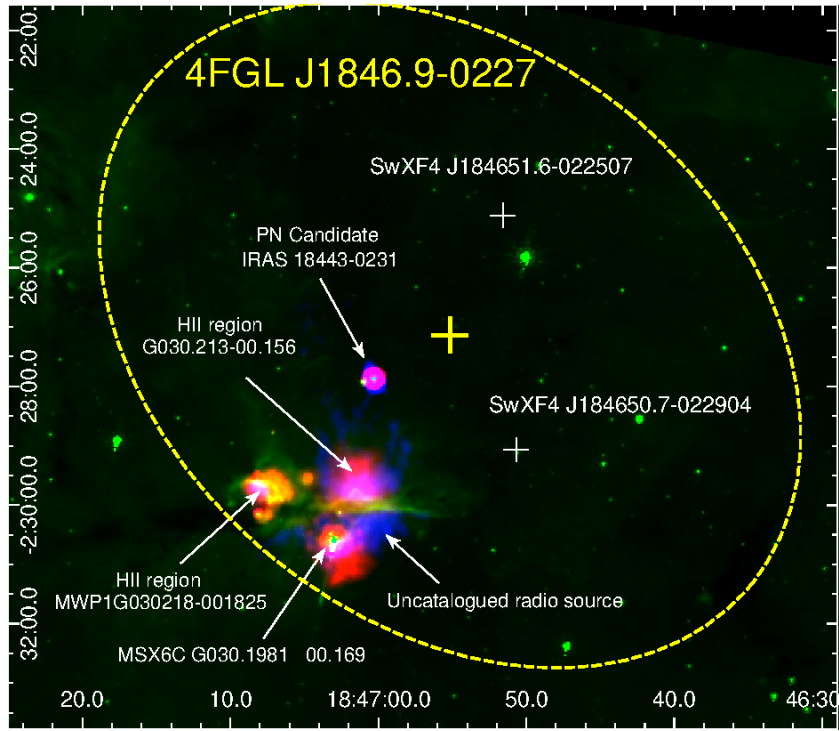


Figure 1. Large scale three color image of the 95% confidence region associated with the Fermi-LAT source 4FGL J1846.9–0227 (dashed-ellipse). The yellow cross indicates the central position of the gamma-ray source. The Spitzer infrared emission at 8 and 24 μm are shown in green and red, respectively, and the MAGPIS radio continuum emission at 20 cm is shown in blue. The main sources in the region are labeled, some of them are candidates for being the counterpart of the Fermi source.

source and the dust filament and the MYSO suggests that this new radio source would be located at the same distance of about 5 kpc of the complex. Both radio sources have 24 μm emission in coincidence with their radio continuum peaks, suggesting that the origin of the uncatalogued source is thermal. However we can not discard that this new radio source is a SNR, which would be of great importance for the study of the origin of the γ -ray emission, hence, we investigate such a source through an spectral index analysis (see Sect. 3.1).

On the other hand, it can also be appreciated two additional compact radio sources in the region, IRAS 18443–0231 and MWP1G030218–001825, which have been cataloged as a possible planetary nebula, and a compact HII region (Anderson et al. 2011), respectively. Given that the nature of IRAS 18443–0231 is still an open issue and it is associated with the X-ray source 4XMM J184700.4–022752, it deserves more analysis in the context of this work (see Sect. 3.5). In such a context, the three X-ray sources indicated in Fig. 2-right panel are analyzed in detail.

In addition, the possible contribution to the γ -ray emission of the MYSO candidate MSX G30 (see Fig. 3), which is embedded in the dust clump AGAL G030.1978–0.1683, is analyzed (see Sect. 3.2).

3.1. The nature of the uncatalogued radio source

In this subsection, we analyze the possibility that the new radio source is a SNR, for which a radio spectral index study is carried out. We use the averaged image between 1.4 and 1.8 GHz from the

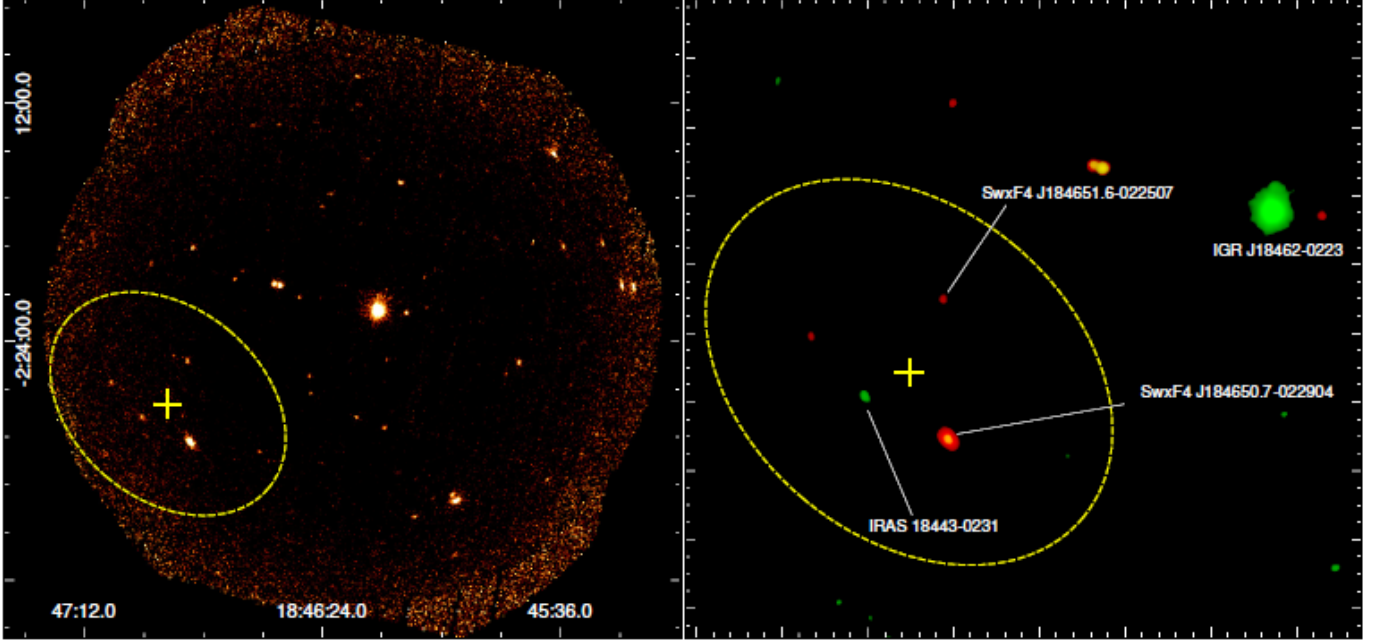


Figure 2. Left: Color-scale shows the whole field of view of the X-ray emission between 0.5 and 8.0 keV from XMM-Newton. Right: Two-color image of the X-ray emission between 0.5 and 2.0 keV (red) and 2.0 and 8.0 keV (green). It is marked the position of IGR J18462–0223 (the original target of the observations), the position of the Swift sources studied by Kerby et al. (2021), whose nature is discussed in this work, and the position of IRAS 18443-0231 which presents considerable hard X-ray emission. The not marked ‘soft source’ within the ellipse, the red one towards the northeast, is related to the HD 173763 star, which is located at a distance of about 330 pc, and it is not considered for our analysis. In both panels, the yellow cross and ellipse indicate the best-fit position and positional error of the Fermi source, respectively.

THOR survey⁴. This image was convolved with a $18'' \times 18''$ (FWHM) Gaussian kernel to match the resolution of the GLOSTAR image.

We obtained the radio continuum fluxes of the HII region G30.21 and the new radio source by integrating the emission over elliptical regions that approximately match the $3.4 \text{ mJy beam}^{-1}$ contour level indicated in Fig. 3-left panel. For the HII region G30.21, we obtained flux densities S_ν of 47 ± 2 and $53 \pm 1 \text{ mJy}$ at 1.6 (THOR) and 5.8 (GLOSTAR) GHz, respectively. For the southern region, we obtained flux densities of 81 ± 2 and $69 \pm 1 \text{ mJy}$ at 1.6 and 5.8 GHz, respectively. The mean noise (rms) at both frequencies is $\sim 1 \text{ mJy beam}^{-1}$ and it was measured over regions free of source emission.

From the flux densities derived above, we calculated radio spectral indexes α ($S_\nu \propto \nu^\alpha$). We obtained $\alpha = 0.10 \pm 0.04$ and -0.12 ± 0.03 for the HII region G30.21 and the southern uncatalogued region, respectively. Our results confirm the thermal nature of the radio emission from HII region G30.21, and strongly suggest that the new radio continuum source is another HII region, named G030.195–00.168 following the naming criteria of Anderson et al. (2015). It is important to mention that this result is consistent with the presence of $24 \mu\text{m}$ emission in positional coincidence with the

⁴ Retrieved from <https://thorserver.mpia.de/data/continuum/>.

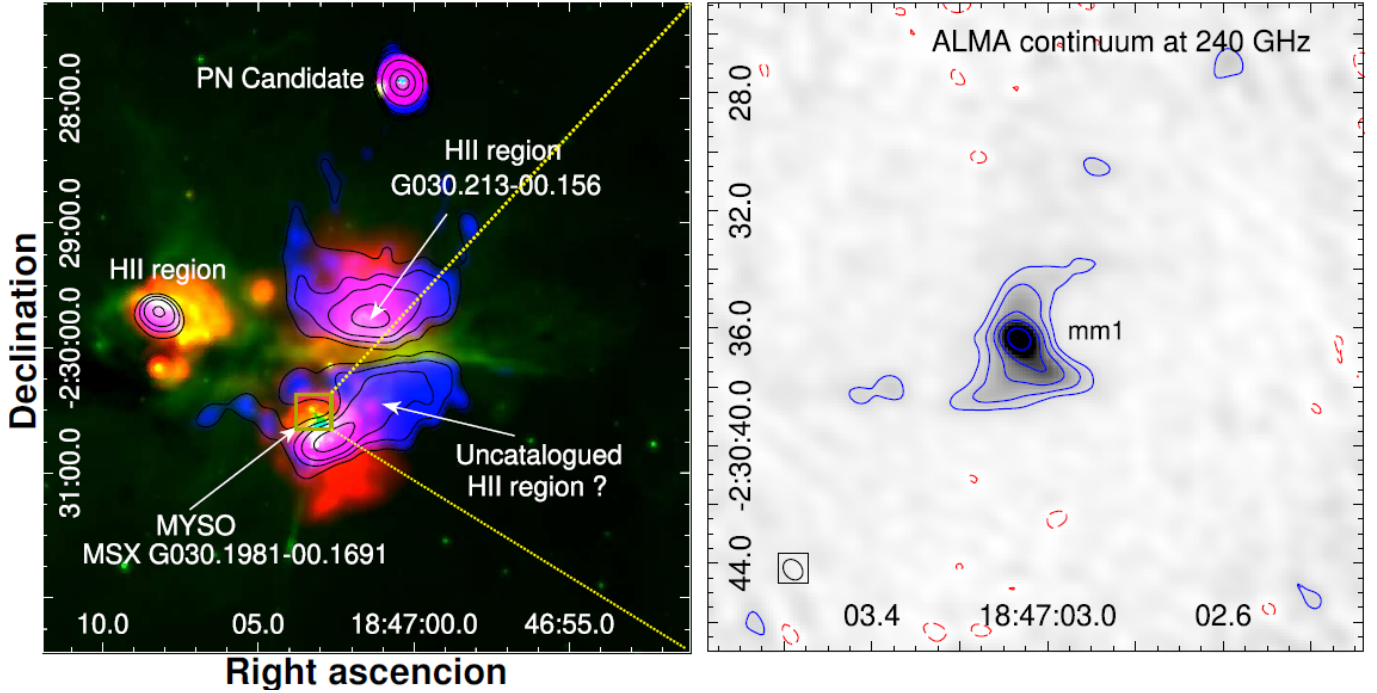


Figure 3. Left panel: Close-up view of Fig. 1 towards the HII regions area. The Spitzer infrared emission at 8 and 24 μm are shown in green and red, respectively, and the MAGPIS radio continuum emission at 20 cm is shown in blue. The black contours highlight the radio continuum emission at 20 cm. Levels are at 3.2, 3.3, 3.4, and 3.5 mJy beam $^{-1}$. Right panel: Grey-scale and blue contours represent the ALMA continuum emission at 1.3 mm. Levels are at 0.5, 2, 5, 8, and 10 mJy beam $^{-1}$. The dashed red contours represent the 3 σ negative continuum emission.

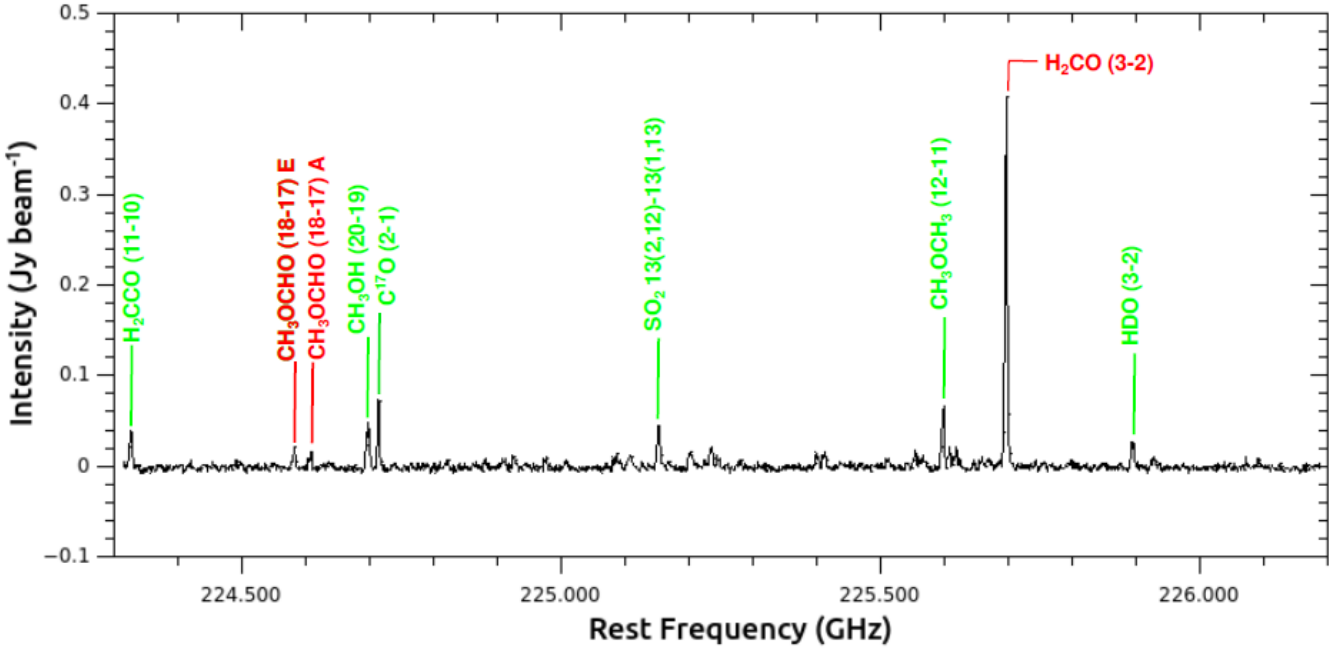


Figure 4. ALMA Band 6 beam averaged spectrum towards the core mm1. The zero moment maps of the red labeled molecules are exhibited in Fig.5.

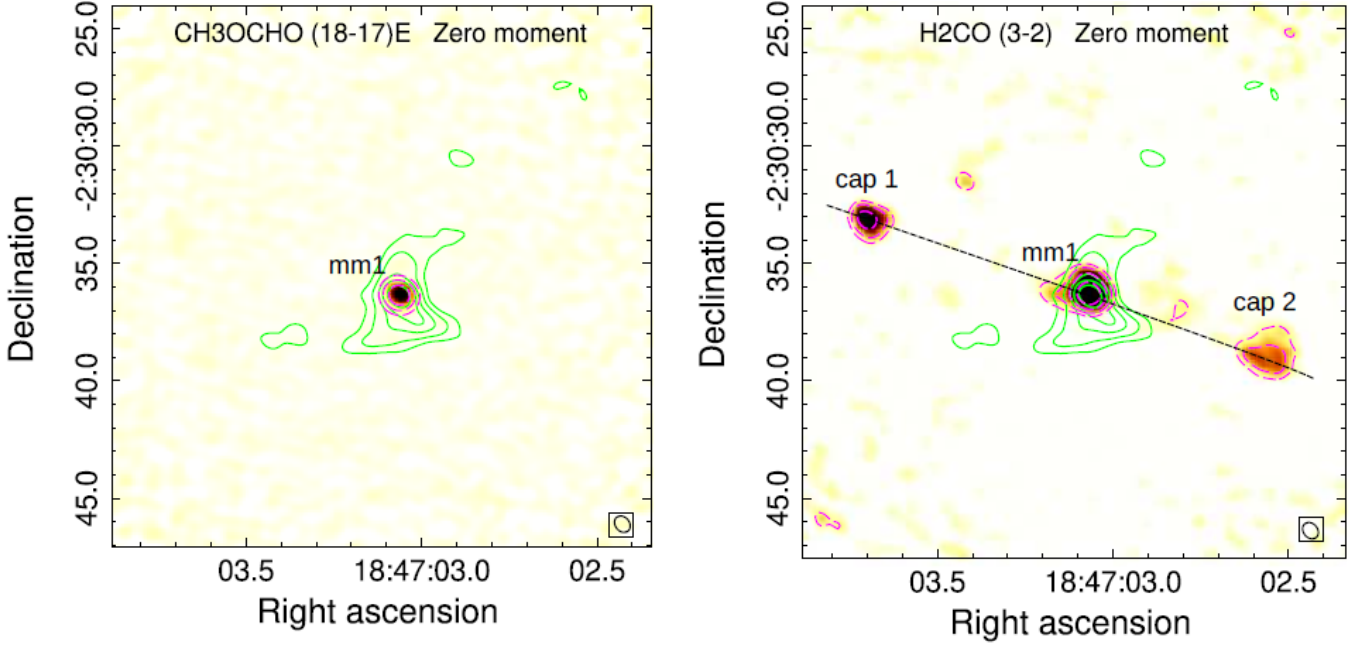


Figure 5. Color-scale and dashed magenta contours show the integrated emissions of the CH₃OCHO (18–17)E (left panel) and H₂CO J=3–2 (right panel) transitions. Levels are at 0.02, 0.04, and 0.07 Jy beam^{−1} and at 0.2, 0.5, 1, and 2 Jy beam^{−1} for CH₃OCHO and H₂CO, respectively. The green contours represent the ALMA continuum emission at 1.3 mm. Levels are at 0.5, 2, 5, 8, and 10 mJy beam^{−1}. The beam of the observation is indicated at the right bottom corner.

1.4 GHz radio continuum emission. Therefore, it seems reasonable to rule out this new radio source as a possible cause of the γ -ray emission.

3.2. The MYSO candidate MSX G30

The MYSO candidate MSX G30 is cataloged as a massive protostar candidate with a bolometric luminosity of about $3 \times 10^4 L_\odot$ (Lumsden et al. 2013). It is well known that MYSOs have associated massive bipolar molecular outflows which can produce strong shocks when interact with the surrounding medium. In these conditions particle acceleration at relativistic velocities can occur leading to gamma ray emission, as some theoretical models predict (Bosch-Ramon et al. 2010, and references therein).

Crossing the Fermi First Year Catalog with some catalogs of MYSO candidates, Munar-Adrover et al. (2011) obtained a list of MYSOs that are spatially coincident with Fermi sources, and therefore, potentially responsible for the γ -ray emission. In particular, the authors found a spatial correlation between the Fermi source 1FGL J1846.8–0233c (a.k.a. 4FGL J1846.9–0227) and MSX G30. Therefore, we searched in the literature for evidence of molecular outflow activity associated with this MYSO candidate.

Using intermediate angular resolution data (about 15'') from the ¹³CO/C¹⁸O (3–2) Heterodyne Inner Milky Way Plane Survey (CHIMPS; Rigby et al. 2016), Yang et al. (2018) searched for massive outflows associated with a sample of 919 ATLASGAL clumps. In particular, the authors did not find any evidence of outflow activity towards the source AGAL G030.1978–0.1683, which is the dust condensation in which MSX G30 is embedded. On the other hand, we searched for Extended

Green Objects (EGOs) in the catalog of Cyganowski et al. (2008). EGOs are usually associated with massive molecular outflow activity. However, there is not any EGOs cataloged in the region.

In this context, we analyzed high resolution and sensitivity continuum and line ALMA data at Band 6 searching for traces of molecular outflow activity at core scale.

Figure 3-right panel shows a close-up view of the MSX G30 region. The gray-scale and blue contours show the ALMA continuum emission at 1.3 mm. It can be seen the presence of a single dust core surrounded by fainter extended emission. The lack of evidence of fragmentation suggests that the bolometric luminosity of about $10^4 L_\odot$ is associated with this single source, which confirms that MSX G30 is indeed a massive protostar.

Figure 4 shows a beam average spectrum ranging from about 224.3 to 226.3 GHz (Band 6) towards the core mm1. Several molecular lines have been detected in this spectral window, but for the purpose of our analysis we will focus on two of them: CH_3OCHO (18,17) and H_2CO (3–2). Figure 5-left panel shows the integrated emission map of CH_3OCHO (18,17) E transition. The spatial distribution of this molecule appears well localized onto the position of the core mm1. The mere presence of this transition, whose typical desorption temperature is about 120 K (e.g. Busch et al. 2022), shows that mm1 is a hot molecular core, which confirms that active star formation is ongoing inside.

Figure 5-right panel shows the integrated emission map of H_2CO J=3–2 transition. It can be seen that the spatial distribution of this molecule exhibits a main peak which perfectly match the position of the core mm1. In addition, it can be noticed two emission features with no associated continuum emission, which are perfectly aligned with the core mm1 (see dotted black line in Fig. 5-right). Taking into account that this molecule usually traces dense gas and molecular outflows (Tychoniec et al. 2021; Okoda et al. 2020), it is very likely that both structures outside the core position are showing signs of outflow activity. In particular, both structures could be tracing the densest gas of the molecular outflows, likely the caps. Given that the velocity difference between both caps are about 3 km s^{-1} , we can infer that the lobes are extended mostly at the plane of the sky. The lineal distance between both caps are about 0.5 pc, which is in agreement with typical outflows sizes.

3.3. Source SwXF4 J184651.6–022507

We note that 4XMM J184651.2–022504 is the XMM-Newton counterpart of the Swift source SwXF4 J184651.6–022507 mentioned in Sect. 1 (see Fig. 2). According to Kerby et al. (2021), this source has an X-ray flux three orders of magnitude smaller than SwF4 J184650.7–022904 (see Sect. 3.4) and it was characterized as a likely blazar.

This faint X-ray source is related to the mid-IR source WISE J184651.22–022505.5 from the All WISE data release Catalog of Cutri et al. (2021). The reported magnitudes for this source in the four mid-IR observed bands are: [3.4]=10.50, [4.6]=10.46, [12.0]=10.08, and [22.0]=5.09 (quality flags AAUB). Even though the quality at the $12 \mu\text{m}$ band indicates that it is an upper limit, it can be used to locate this source in a color-color ([3.4]–[4.6] vs. [4.6]–[12.0]) diagram. This kind of diagrams are very frequently used to determine a blazar association (e.g. D’Abrusco et al. 2012). The source lies very far from the blazars region in such a diagram, in fact, it is located in the region in which the stars are expected to be. Moreover, giving that the source lies very close to the galactic plane ($l = -0.08 \text{ deg}$), a galactic origin is more likely. Hence, we discard the blazar nature and its responsibility for the high-energy emission.

3.4. Source *SwXF4 J184650.7-022904*

Source 4XMM J184650.6–022907 is the XMM-Newton counterpart of the Swift source SwXF4 J184650.7–022904 (see Fig. 2). According to the XMM-Newton Serendipitous Source Catalog, Thirteenth Data Release⁵ (4XMM-DR13), this source presents significant variability: the EPIC count-rate between 0.2 and 12 keV increases from $(9.0 \pm 0.4) \times 10^{-2}$ ctss $^{-1}$ for Obs1 (2011) to $(17.4 \pm 0.6) \times 10^{-2}$ ctss $^{-1}$ for observation Obs2 (2018).

Looking for possible counterparts of 4XMM J184650.6–022907, we found that it is related to mid-IR source WISE J184650.7-022904 (Cutri et al. 2021) with magnitudes [3.4]=8.861, [4.6]=6.951, [12.0]=7.108, and [22.0]=8.106 (quality flags AAAU). Again, from a color-color ([3.4]-[4.6] vs. [4.6]-[12.0]) diagram, this source is not compatible with a blazar. We also found that the star BD–02 4739 (at 18:46:50.69 –02:29:07.30, J2000), cataloged as a spectroscopic binary in the Non-single stars Catalog by GAIA DR3 (Gaia Collaboration 2022), is considered the optical counterpart in the 4XMM-DR13 catalog. Indeed, it lies at the same coordinate of 4XMM J184650.6–022907 within a positional difference less than 0.1 arcsec (see Fig. 6). Taking into account this perfect positional coincidence, it is very likely that both sources are related, and hence, it deserves more analysis in the context of this work.

3.4.1. Spectroscopic binary star BD–02 4739

As noted in previous section, it is very likely that the spectroscopic binary star BD–02 4739 is the optical counterpart of 4XMM J184650.6–022907. The distance and orbital period reported by GAIA DR3 are 452 ± 12 pc and 53 d, respectively (Gaia Collaboration 2022). Several other optical/ir associations are reported in the 4XMM-DR13 catalog and Simbad for this star, which are useful to determine its spectral type through a spectral energy distribution (SED) analysis.

In a binary system, in principle both components contribute to the fluxes observed at different wavelengths, hence a SED study must be done with care. In this case, we conducted a SED analysis based on the statement that one of the components of this binary system should be a black hole, a neutron star or a white dwarf, issue discussed in Sect. 4, and hence we assume that the analyzed fluxes for the SED came mainly from a donor stellar companion.

In Table 2 we report the associated sources from the WISE Source Catalog (AllWISE, band W4 is excluded because the flux is reported as an upper limit), the Galactic Legacy Infrared Mid-Plane Survey Extraordinaire (GLIMPSE) performed with the Spitzer Space Telescope, the Two Micron All-Sky Survey (2MASS), the GAIA Data Release 3 (Gaia DR3), the Tycho 2 Main Catalog (Tycho-2), and the XMM-Newton Optical Monitor (XMM-OM) Source Catalog (XMM-SUSS5.0). We have excluded the optical source 1237668687974826071 from the Sloan Digital Sky Survey Data Release 12 (SDSS DR12) because several photometric flags are reported. Flux densities (f_λ) were calculated from the magnitudes m reported in the catalogs as $F_\lambda = F_0 10^{-0.4m}$, where F_0 is the zero-point flux, whose values were obtained from Rodrigo & Solano (2020).

We fit the spectral energy distribution (SED) using a black-body function without interstellar extinction, a reasonable approximation taking into account the proximity of the source. The fit

⁵ Catalog available through the XMM-Newton Science Archive interface at <https://www.cosmos.esa.int/web/xmm-newton/xsa>

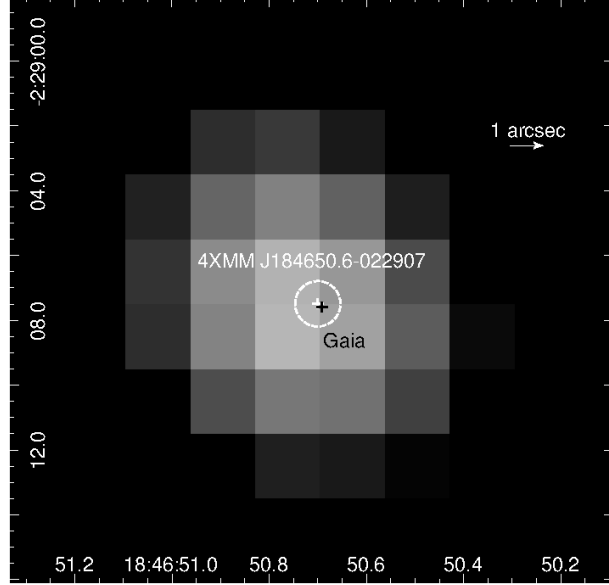


Figure 6. Zoom-in of the exposure-corrected image of **Fig. 1 (right)**. The white cross and circle are the position and positional error of 4XMM J184560.6–022907 reported in the 4XMM-DR13 catalog, respectively. The position of the spectroscopic binary star BD–02 4739 from Gaia DR3 is marked with a black cross.

Table 2. Optical and infrared counterparts of 4XMM J184650.6–022907 and the flux densities at different filters.

Survey / Source ID	Filter / λ [μm]	f_λ [erg s ⁻¹ cm ⁻² Å ⁻¹]
allWISE /	W1 / 3.35	$1.42 \pm 0.04 \times 10^{-14}$
184650.68–022907.4	W2 / 4.60	$4.03 \pm 0.08 \times 10^{-15}$
	W3 / 11.56	$1.01 \pm 0.06 \times 10^{-16}$
Spitzer GLIMPSE /	IRAC 3.6 / 3.54	$1.01 \pm 0.02 \times 10^{-14}$
G030.1965–00.111	IRAC 4.5 / 4.48	$4.19 \pm 0.17 \times 10^{-15}$
	IRAC 5.8 / 5.70	$1.87 \pm 0.05 \times 10^{-15}$
	IRAC 8.0 / 7.80	$5.55 \pm 0.15 \times 10^{-16}$
2MASS /	J / 1.24	$2.30 \pm 0.06 \times 10^{-13}$
18465069–0229072	H / 1.65	$1.47 \pm 0.04 \times 10^{-13}$
	Ks / 2.16	$6.56 \pm 0.10 \times 10^{-14}$
Gaia DR3 /	BP / 0.51	$2.12 \pm 0.01 \times 10^{-13}$
4259072330161989504	G / 0.62	$2.73 \pm 0.01 \times 10^{-13}$
	RP / 0.77	$3.17 \pm 0.01 \times 10^{-13}$
Tycho-2 /	B / 0.42	$1.11 \pm 0.10 \times 10^{-13}$
TYC2 5118-160-1	V / 0.53	$2.32 \pm 0.10 \times 10^{-13}$
XMM-OM /	UVM2 / 0.23	$1.24 \pm 0.03 \times 10^{-15}$
50813589		

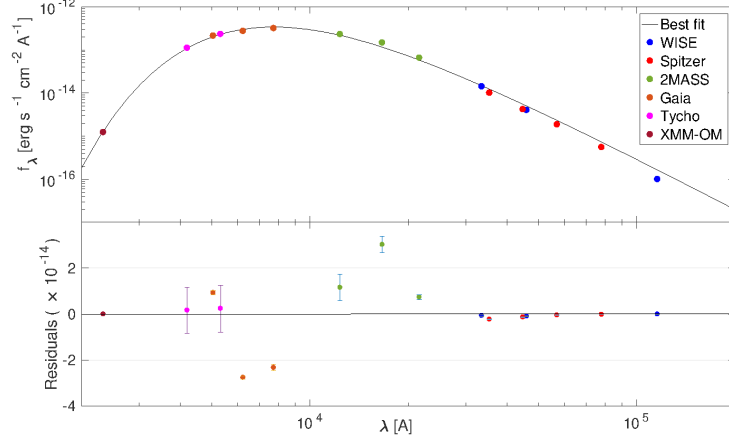


Figure 7. UV, optical and infrared flux densities and the best fit with a pure black-body function without interstellar extinction. The error bars are only shown in the residuals plot.

parameters are the effective temperature T_{eff} and the dimensionless normalization A :

$$f_\lambda = A \frac{2hc^2}{\lambda^5} \frac{1}{\exp(hc/\lambda kT_{eff}) - 1}, \quad (1)$$

where λ is the wavelength, c the light speed, k the Boltzmann constant and h the Planck constant. The normalization A is related with the angular size of the source θ ,

$$\theta = \frac{R}{D} = \sqrt{\frac{A}{\pi}}, \quad (2)$$

where R is the radius and D the distance. In Fig. 7 we show the fluxes of Table 2 and the result of the fit. We obtain $T_{eff} = 3800 \pm 40$ K and $A = (9.50 \pm 0.64) \times 10^{-27}$ (errors correspond to 90% confident level). Using Eq. 2 we obtain a stellar radius of about $11 R_\odot$.

We estimate the flux by numerically integrating f_λ between $\lambda = 0$ and ∞ and obtain $F = 3.6 \pm 0.3 \times 10^{-9}$ erg s $^{-1}$ cm $^{-2}$. The bolometric luminosity is estimated from the relation $L = 4\pi D^2 F = 23 \pm 2$ L $_\odot$. To determine the spectral type of BD-02 4739, we construct the HR diagram of Fig. 8, where we include the location of the main sequence, sub-giant, and giant stars, corresponding to luminosity classes V, IV and, III, respectively (taken from de Jager & Nieuwenhuijzen 1987).

Hence, we suggest that the donor star, this is, the member that would contribute the most to the IR and optical fluxes, should be a low-mass star out of the main sequence, likely a sub-giant star.

3.4.2. X-ray spectral analysis

We extracted the X-ray spectra of 4XMM J184650.6–022907 from the 3 cameras of each XMM-Newton observation, yielding to a set of 6 spectra. The source extraction region was a circle of 24" in radius and background spectra were extracted from nearby circular regions in the same CCD as the source region. We use the *evselect* task of SAS with a minimum of 15 counts per bin. We obtained 209 (mos1), 245 (mos2), and 416 (pn) counts for observation Obs1, and 359 (mos1), 391 (mos2), and 415 (pn) counts for Obs2, in the 0.5–3.0 keV energy band. The spectra were displayed and analyzed with the Xspec software (version 12.14.0), which is included in the HEASoft package.

We visually inspected the 6 spectra and found X-ray emission coming from a soft and featureless continuum, without evidence of spectral lines (Fig. 9). We note, however, that the absence of lines in

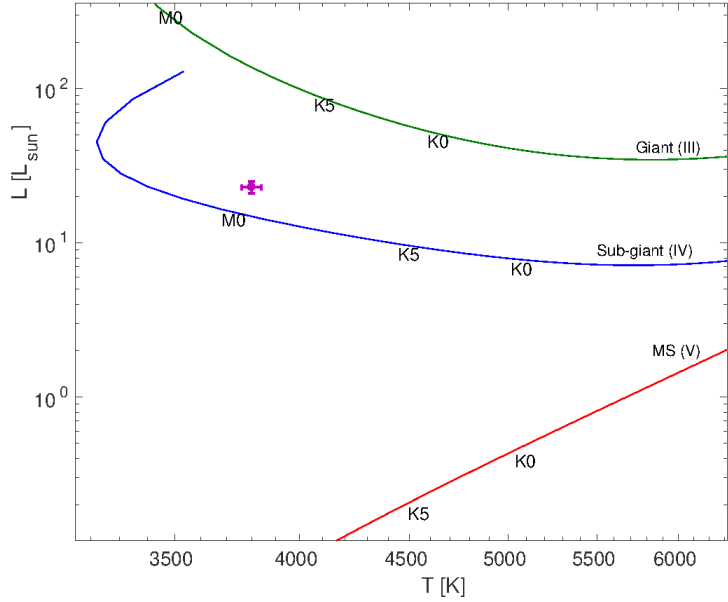


Figure 8. HR diagram with the main sequence (MS), sub-giant, and giant luminosity classes. The point corresponds to the position of BD-02 4739.

the spectra may be a consequence of the relative low number of counts and the binning. We first fit each observation separately with different emission models in the $0.5 - 3.0$ keV energy band, to look for possible variations of model parameters between Obs1 and Obs2. To explore the non-thermal scenario we use an absorbed power law ($tbabs \times powerlaw$). We obtain an unrealistic soft photon index ($\Gamma_X \sim 8$ and ~ 5 for Obs1 and Obs2, respectively) and a quite poor fit ($\chi^2 \sim 1.4$ and 1.8 , for Obs1 and Obs2)⁶. To explore the thermal nature of the source, we fitted the spectra with a blackbody, a bremsstrahlung, and an optically thin plasma. We obtained poor results for the blackbody ($\chi^2 \sim 1.6$ and 2.0 , for Obs1 and Obs2) and bremsstrahlung ($\chi^2 \sim 2$ for Obs1 and Obs2), and an acceptable fit for the thin plasma ($tbabs \times apec$). For this model, the 90% confidence range for the hydrogen column densities are $N(H) \sim (0.23 - 0.53) \times 10^{22} \text{ cm}^{-2}$ (Obs1) and $\sim (0.24 - 0.40) \times 10^{22} \text{ cm}^{-2}$ (Obs2), showing no significant variation of the absorbing material between observations. For the electron temperature (kT), we obtain confidence ranges $0.71 - 0.85$ keV (Obs1) and $0.87 - 1.04$ keV (Obs2), implying a slightly warmer plasma for Obs2. Metal abundance (*Abund.*) is sub-solar and confidence ranges are $0.12 - 0.74$ for Obs1 and $0.07 - 0.16$ for Obs2.

Based on the results of the individual fit of each observation, and in order to increase the fit statistic, we simultaneously fit Obs1 and Obs2 spectra using a thermal plasma model with the same $N(H)$. In Table 3 we show the fitting results for the absorbed thermal plasma, considering two procedures: i) all parameters except normalization are tie together between Obs1 and Obs2, and ii) only N_H is tie together between the observations.

The results of the spectral fitting reported in Table 3 show that the X-ray emission from 4XMM J184650.6-022907 is likely produced by a thermal plasma with a temperature $\lesssim 1$ keV and sub-solar abundance. There is a slight increase in the plasma temperature between observations (refer to the

⁶ To characterize the goodness of the fit, we report the reduced χ^2 , i.e. $\chi^2_r = \chi^2/\text{d.o.f.}$, where *d.o.f.* are the degrees of freedom.

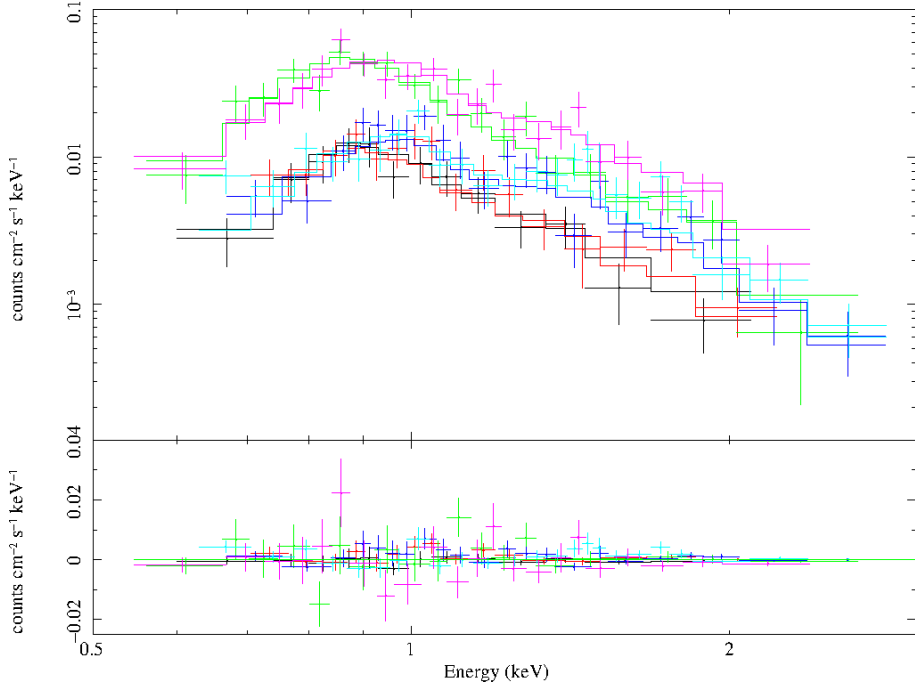


Figure 9. X-ray spectra of the point source 4XMM J184650.6–022907 between 0.5 and 3.0 keV, for XMM-Newton observations Obs1 (mos1: black, mos2: red, pn: green) and Obs2 (mos1: blue, mos2: cyan, pn: magenta). The solid lines correspond to the best fit absorbed thermal plasma ($tbabs \times apec$) with N_H tied together between observations and all the remaining parameters let to vary free.

Table 3. Best fit parameters for the optically thin plasma ($tbabs \times apec$) for 4XMM J184650.6-022907. The “=” symbol indicates that the corresponding parameter for Obs2 is set equal to Obs1 during the fitting procedure. *Abund.* is the metal abundance relative to the Sun and η is the normalization, defined as the emission measured of the gas scaled by the distance: $\eta = 10^{-14} \int n_e n_H dV / (4\pi D^2)$, where electron and proton densities are expressed in cm^{-3} , the gas volume element dV in cm^3 , and the source distance D in cm. F_X and L_X are the flux and luminosity corrected for absorption in the 0.5 – 3.0 keV energy band, respectively. L_X is calculated for a distance of 452 pc.

Parameter	Obs1	Obs2	Obs1	Obs2
χ^2_r	1.27		1.04	
$N(\text{H}) (\times 10^{22} \text{ cm}^{-2})$	$0.28^{+0.13}_{-0.05}$	=	$0.32^{+0.08}_{-0.06}$	=
kT (keV)	$0.91^{+0.06}_{-0.12}$	=	$0.79^{+0.06}_{-0.06}$	$0.96^{+0.07}_{-0.09}$
<i>Abund.</i>	$0.12^{+0.04}_{-0.03}$	=	$0.19^{+0.15}_{-0.07}$	$0.11^{+0.05}_{-0.04}$
$\eta (\times 10^{-4})$	$2.26^{+0.80}_{-0.39}$	$4.27^{+1.20}_{-0.75}$	$2.04^{+0.67}_{-0.58}$	$4.92^{+1.30}_{-0.92}$
$F_X (\times 10^{-13} \text{ erg s}^{-1} \text{ cm}^{-2})$	$1.52^{+0.59}_{-0.21}$	$2.87^{+1.08}_{-0.39}$	$1.72^{+0.41}_{-0.28}$	$3.13^{+0.61}_{-0.45}$
$L_X (\times 10^{30} \text{ erg s}^{-1})$	$3.72^{+1.44}_{-0.51}$	$7.01^{+0.95}_{-2.64}$	$4.21^{+0.69}_{-0.99}$	$7.64^{+1.09}_{-1.51}$

right column of the Table), and no significant variations of the metal abundance. The normalization increases by a factor ~ 2 between observations, i.e. in a time scale of 7 years. This indicates that the increase of the flux is produced by an increase of the amount of emitting plasma.

3.5. PN candidate IRAS 18443-0231

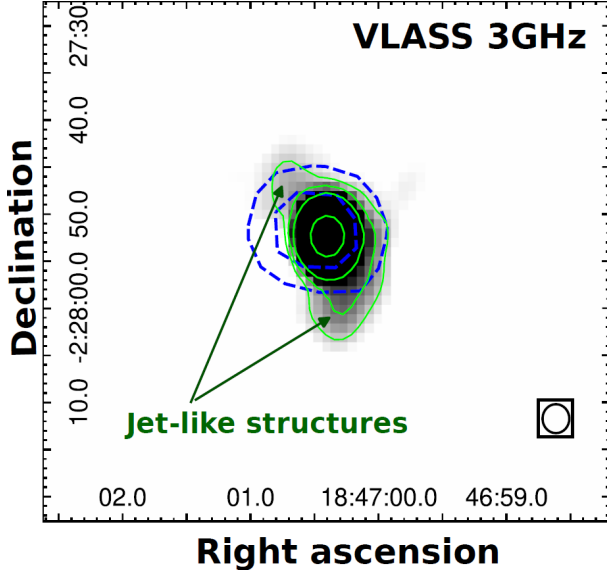


Figure 10. Grey-scale and green contours show the radio continuum emission at 3 GHz toward IRAS 18443–0231 extracted from VLASS. Levels are at 2 (5σ), 4, 10, and 80 mJy beam $^{-1}$. Blue-dashed contours represent the continuum emission at 850 μ m extracted from SCUBA. Levels are at 1.0 and 1.6×10^{-4} pW. The beam of the radio continuum at 3 GHz is indicated at the bottom right corner

IRAS 18443-0231 appears as a planetary nebula candidate in the Simbad Catalog. It is located at the far kinematic distance of about 8 kpc with a systemic velocity of 110 km s $^{-1}$ (see for instance Yang et al. 2016; Irabor et al. 2018). By analyzing the spectrum of the H₂O maser from Urquhart et al. (2011), we point out that this source could be a “water-fountain” PN, which is indeed a very interesting kind of object due to the scarce of them (e.g. Boboltz & Marvel 2005; Fan et al. 2024). As was mentioned in Section 1, 4FGL-DR3 and 4FGL-DR4 Fermi catalogs refer to the radio source TXS 1844–025 (18:47:00.5, -02:27:52, J2000), which is indeed IRAS 18443–0231, as a ‘possible association’. Thus, we conclude that such a source deserves a thorough analysis in the context of this work.

Figure 10 presents in grey and green contours the radio continuum emission at 3 GHz towards the PN candidate IRAS 18443–0231. The blue-dashed contours represent the SCUBA continuum emission of cold dust at 850 μ m. The centimeter and submillimeter radio sources show a very good spatial correlation. Strikingly, the 3 GHz emission exhibits faint extended structure, whose morphology resembles jets arising from the central source.

Using the integrated flux densities at 1.4, 3.0, and 5.0 GHz, after convolving VLASS and CORNISH images to the lower resolution of the MAGPIS image, we estimate the radio spectra index α ($S_\nu \propto \nu^\alpha$), obtaining a negative index value of -0.47 ± 0.08 (see Fig. 11) for the whole source. In all cases the source size is smaller than the largest angular scale of each observation, therefore the radio flux should be completely recovered for the three frequencies. The background subtraction was about 5% in the MAGPIS image and negligible in the VLASS and CORNISH images. Thus, we found non-thermal radio continuum emission associated with IRAS 18443–0231, which indicates the presence of synchrotron particle acceleration related to jets, strongly suggesting that the source is a protoplanetary nebula (pPN).

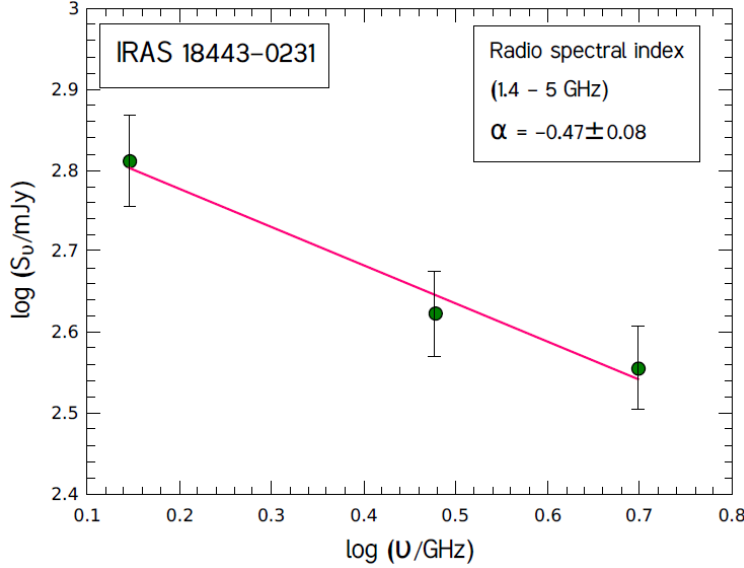


Figure 11. Flux density as a function of frequency for IRAS 18443-0231. Error bars are an assumed uncertainty of 10% from the flux densities. The red line is the best fit to the data from a power law of the form $S_\nu \propto \nu^\alpha$.

The 850 μm emission (see blue-dashed contours in Fig. 10) suggests that IRAS 18443-0231 is embedded in a molecular clump. Hence, we roughly estimate the mass of gas from the cold dust emission as usually is done using the formula:

$$M = \frac{F_\nu d^2}{k_\nu B_\nu(T_d)}, \quad (3)$$

where F_ν is the integrated flux density (we obtain 0.12 Jy), d the distance to the source (assumed in 8 kpc), k_ν the dust opacity per gram of matter (we used $0.0185 \text{ cm}^2 \text{g}^{-1}$) and $B_\nu(T_d)$ is the Plank function with T_d the dust temperature (assumed in 20 K). We obtained a mass and density about 140 M_\odot and 10^3 cm^{-3} .

Additionally, we looked for molecular outflows towards this source. Using data from the JCMT we found a spectral wing in the ^{12}CO $J=3-2$ spectrum suggesting the presence of a red-shifted outflow (see Fig. 12). It can be noticed that if there was a blue-shifted outflow it would be masked within the ^{12}CO component centered at 95 kms^{-1} , which correspond to foreground molecular gas. Figure 13 displays in red contours the ^{12}CO emission integrated between 115 and 130 kms^{-1} (i.e. along the spectral wing shown in Fig. 12) and clearly shows the presence of a lobe corresponding to a red-shifted molecular outflow emanating from IRAS 18443-0231.

Figure 14 shows the good spatial correlation between the radio continuum emission at 3 GHz associated with the protoplanetary nebula IRAS 18443-0231 and the X-ray source 4XMM J184700.4-022752. Moreover, it can be appreciated a diffuse extended structure toward the southwest in the X-ray emission, which seems to accompany the direction of the red lobe of the ^{12}CO (3-2) molecular outflow.

3.5.1. X-ray analysis of IRAS 18443-0231

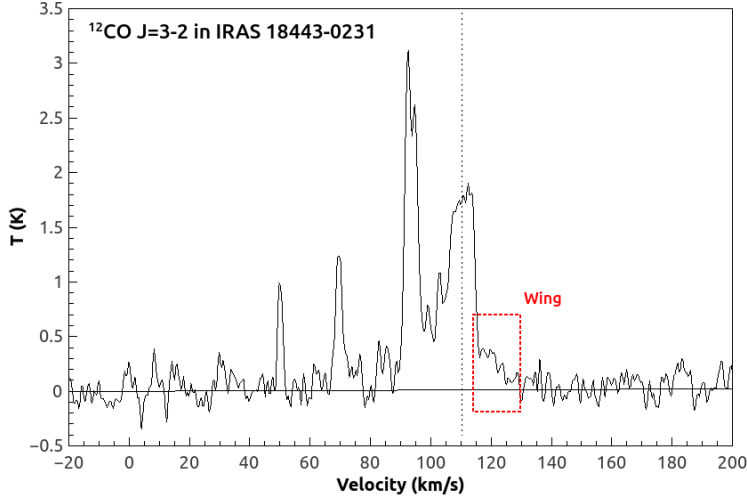


Figure 12. ^{12}CO $J=3-2$ spectrum obtained toward IRAS 18443-0231. The spectral wing indicating a red-shifted molecular outflow is marked. The vertical dotted line represents the systemic velocity of the source.

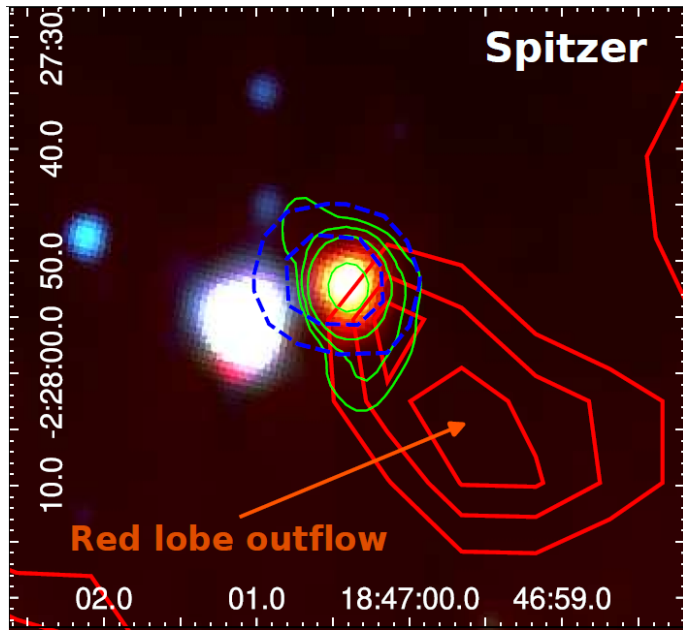


Figure 13. Three-color Spitzer image toward IRAS 18443-0231 with 3.6, 4.5, and $8\text{ }\mu\text{m}$ emissions represented in blue, green, and red, respectively. The green and blue-dashed contours are the same ones that were presented in Fig. 10. The red contours represent the ^{12}CO $J=3-2$ emission integrated between 115 and 130 km s^{-1} . Levels are at 8, 11, and 14 K km s^{-1} .

4XMM J184700.4–022752 is a hard X-ray source, with most of the photons detected between 2.0 and 6.0 keV. The reported count rate in the pn cameras are $1.65 \pm 0.33 \times 10^3\text{ cts s}^{-1}$ and $1.49 \pm 0.24 \times 10^3\text{ cts s}^{-1}$ for Obs1 and Obs2, respectively, indicating a constant flux between observations (refer to the 4XMM-DR13 catalog). To analyze the X-ray emission from 4XMM J184700.4–022752, we extracted source and background spectra from the 6 available cameras. We obtained 289 source counts, which in principle is sufficient for a spectral fitting. Taking into account the lack of variability,

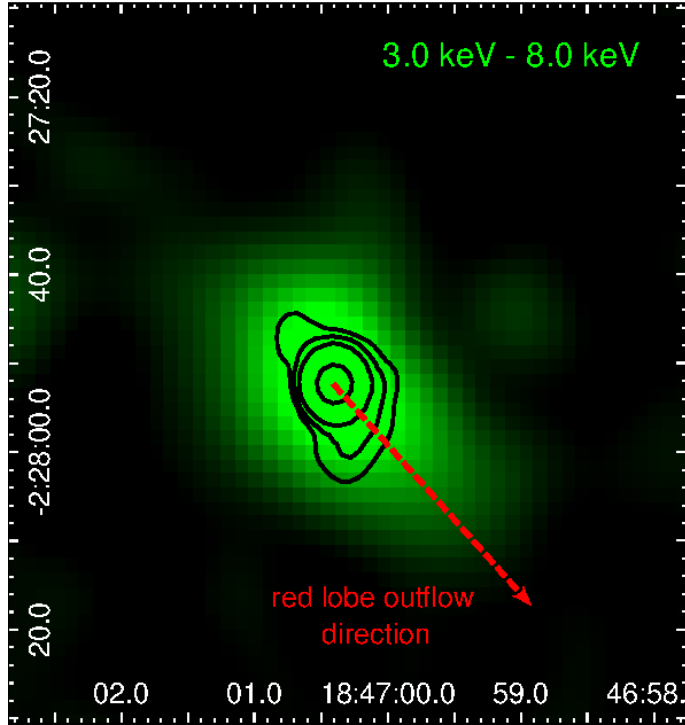


Figure 14. X-ray emission between 3.0 and 8.0 keV associated with the source 4XMM J184700.4–022752 (IRAS 18443-0231) displayed in green. The black contours correspond to the 3 GHz radio continuum emission related to IRAS 18443–0231. Levels are at 2 (5 σ), 4, 10, and 80 mJy beam $^{-1}$. The direction of the red lobe outflow shown in Fig. 13 is indicated with the red arrow.

we combined the source spectra of the 6 cameras into a single spectrum using the *epicspeccombine* task of SAS. The merged spectrum was binned with a minimum of 15 counts per bin. We used Xspec to display and analyze the spectrum. We fitted the spectrum using different emission models to determine whether the emission has a thermal or non-thermal nature.

Unfortunately, we could not determine the best-fit model based on the χ^2_r and the model parameters had large uncertainties. Then, for the purpose of estimating the X-ray flux of the source, we assume some spectral behavior. Taking into account that the radio emission of the pPN is likely produced by synchrotron radiation and has a spectral index $\alpha \sim -0.5$, we consider an absorbed power law ($tbabs \times powerlaw$) in the X-ray band with a fixed photon index $\Gamma_X = 1 - \alpha = 1.5$. In other words, we are assuming that the non-thermal radio emission extends to the X-ray domain without a spectral break. We fitted the spectrum on the 1.0 – 7.0 keV energy band letting the absorption ($N(\text{H})$) and normalization ($Norm$) as free parameters. We obtained $N(\text{H}) = 5.4_{-1.3}^{+1.7} \times 10^{22} \text{ cm}^{-2}$, and $Norm = 2.45_{-0.32}^{+0.58}$ and $\chi^2 = 1.02$ for 19 d.o.f. In Fig. 15 we show the merged spectrum and the best fit powerlaw model. The unabsorbed flux in the 1.0 – 7.0 keV band is $1.3 \pm 0.3 \times 10^{-13} \text{ erg s}^{-1} \text{ cm}^{-2}$ and the luminosity for a distance of 8 kpc is $9.9 \pm 2.0 \times 10^{32} \text{ erg s}^{-1}$. This value could be compatible with the expected non-thermal X-ray luminosity in very young pPNe (Blackman et al. 2001; Sahai et al. 2003).

4. DISCUSSION ABOUT THE NATURE OF THE GAMMA-RAY EMISSION

In this section, the nature of the gamma-ray source 4FGL J1846.9–0227 is discussed based on the previous multiwavelength characterization of the region.

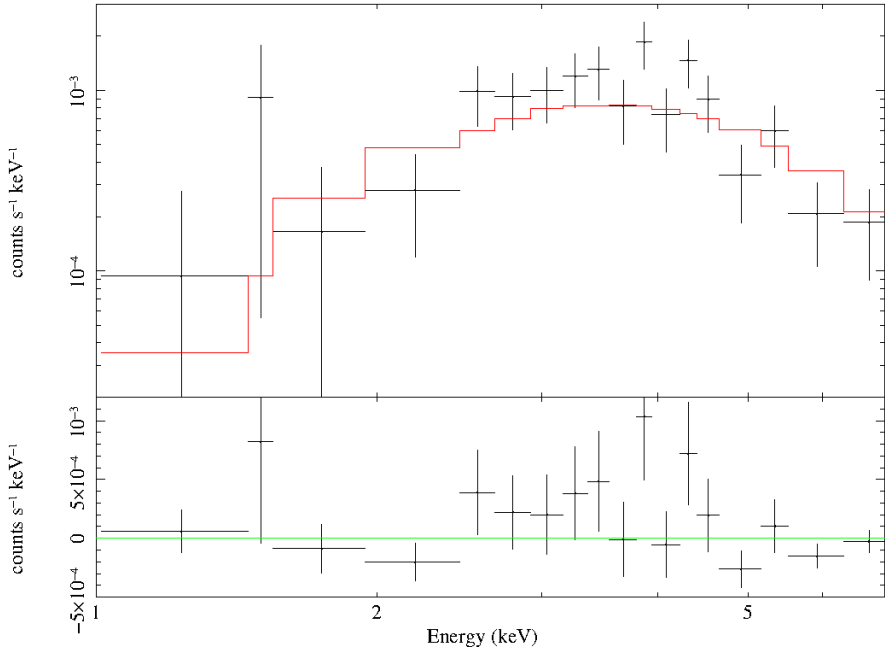


Figure 15. X-ray spectrum of 4XMM J184700.4–022752 between 1.0 and 7.0 keV, obtained by combining the 6 individual available spectra of Obs1 and Obs2. The best-fit absorbed powerlaw for a photon index $\Gamma_X = 1.5$ is shown in red.

4.1. Is 4FGL J1846.9–0227 a blazar?

Kerby et al. (2021) analyzed a sample of 174 unidentified Fermi sources with a single X-ray/UV/optical counterpart. Given that the majority of the sources of 4FGL catalog are pulsars and blazars, the authors developed a neural network classifier approach using gamma-ray, X-ray, and UV/optical spectral parameters to yield a descriptive classification of unassociated spectra into pulsars and blazars. The study included the Fermi-LAT source 4FGL J1846.9–0227, but for the reasons mentioned in Sect. 1, the association of this gamma-ray source with a blazar was ambiguous, which encouraged us to carry out a more in-depth study of the source.

First of all, the location of 4FGL J1846.9–0227, close to the galactic plane ($b \sim -0^\circ 16$), would suggest a galactic origin for the high energy source. Then, as shown above, we discarded the blazar nature of the the X-ray sources indicated by Kerby et al. (2021). It is worth noting that the X-ray emission of the most intense one, that it is related to 4XMM J184650.6–022907, was modeled by an optically thin thermal plasma (see Sect. 3.4.2). This indeed discards a blazar as a possible counterpart, given that these extra-galactic sources typically produce non-thermal X-rays via the synchrotron mechanism (Kaur et al. 2019; Kerby et al. 2021).

In conclusion, 4XMM J184650.6–022907 related to a binary system and the source IRAS 18443–0231 are the best candidates to focus our attention to try to explain the high-energy emission.

4.2. Relating 4XMM J184650.6–022907 with the binary star BD–02 4739

Having ruled out a blazar as possible counterpart of 4XMM J184650.6–022907, the connection between the X-ray source and the spectroscopic binary star BD–02 4739 is important in the context of this work. As mentioned before, Fig. 6 shows the very good spatial correlation between BD–02 4739 and 4XMM J184650.6–022907, which strongly suggests the connection between both sources.

In what follows, we explore different scenarios to explain the X-ray emission arising from the binary star.

4.2.1. *X-ray binaries*

X-ray binaries (XRBs) are binaries system composed by an accreting compact object, a neutron star or a black hole, orbiting a companion, or donor star, from which it accretes material. This material is accelerated in the strong gravitational field of the compact object and heated up to about 10^7 K before being accreted, giving as a result the observed X-ray radiation. The basic division of XRBs into the high-mass (HMXBs) and low-mass (LMXBs) systems depends on the mass of the donor star. While the donor of LMXBs is a low-mass star, typically with masses $\lesssim 1 M_\odot$, the masses of donor stars in HMXBs systems are $\gtrsim 10 M_\odot$.

In most HMXBs, the compact object usually is a neutron star, which accretes material from the stellar wind of its massive companion (Liu et al. 2006). High-mass stars have powerful stellar winds with mass loss rates $\gtrsim 10^{-6} M_\odot \text{yr}^{-1}$ (Smith 2014), so direct wind accretion usually results in high accretion rates, producing X-ray luminosities in the $10^{35} - 10^{40} \text{ erg s}^{-1}$ range (Fornasini et al. 2023). The donor star in most HMXBs is either a supergiant O/B star or a Be star, both of which have higher mass loss rates than O/B main sequence stars. The HMXBs typically have bright X-ray hard spectrum, which can be adequately modeled by a power law (Haberl et al. 2022; Sidoli & Paizis 2018), however, some of them exhibit a small excess of soft X-rays whose origin is not entirely clear (van der Meer et al. 2005). Therefore, taking into account that the X-ray luminosity of 4XMM J184650.6–02290 is about $10^{30} \text{ erg s}^{-1}$, that its soft X-ray spectrum is well fitted by an optically thin thermal plasma model, and finally, that the optical/IR SED indicates that the donor companion is a low-mass star (an M0 sub-giant), we can rule out that the binary BD–02 4739 is a HMXB.

On the other hand, LMXBs are typically less bright than HMXBs, with X-ray luminosities that can be as low as $10^{30} \text{ erg s}^{-1}$ for quiescent systems in which little or no accretion occurs (Bahramian & Degenaar 2023). Therefore, at least from the X-ray luminosity point of view, we cannot rule out that 4XMM J184650.6–022907 is a LMXB. Moreover, the spectral type of the donor star, a M0 sub-giant star, is consistent with LMXBs. However, X-ray emission from LMXBs is not expected to be produced by an optically thin thermal plasma, as we found for 4XMM J184650.6–022907. The spectral emission of LMXBs can be composed of three main components: disk blackbody originating from optically-thick accretion disc, a comptonized component originating due to comptonization of X-rays in the corona, and eventually, a blackbody component of emission from the neutron star surface or the boundary layer (Lin et al. 2009). Regarding energy spectra modeling of LMXBs, there are two different approaches: (1) a soft/thermal, and (2) a hard/comptonized components (Mitsuda et al. 1989; Hasinger & van der Klis 1989), typically fitted by blackbody and power-law models (Abdelfatah et al. 2021), respectively. In summary, given the behavior of the X-ray spectrum of 4XMM J184650.6–022907 it is unlikely that the X-ray emission is originated in a LMXB.

4.2.2. *A symbiotic binary system*

We investigated the possibility that the X-ray emission is being originated by a symbiotic binary system. Such kind of sources are wide binary systems in which a compact object, usually a white dwarf (WD), accretes from a more evolved companion, typically a red giant.

The bolometric luminosity of an accreting WD with a red giant companion is set mainly by whether or not accreted material burns quasi-steadily in a shell on the surface of the WD. During the shell

burning stage the luminosity of the WD is typically $10^3 L_\odot$, but if shell burning is absent, its luminosity is of the order of $10 L_\odot$ (Sokoloski et al. 2016). Taking into account that in absence of shell burning, the red giant, and in some cases the accretion disk, dominates the optical spectrum (Sokoloski et al. 2016), the bolometric luminosity derived in Sect. 3.4.1 for BD–02 4739 star of about $23 L_\odot$ is consistent with a scenario of a WD-symbiotic with non shell burning.

It is worth noting that the X-ray emission from 4XMM J184650.6–022907 is also compatible with the so-called β -type symbiotics, first introduced by Muerset et al. (1997). This class is characterized by soft emission produced by photons with energies less than $\sim 2 - 3$ keV. According to Sokoloski et al. (2016), both burning and non-burning symbiotics may belong to the β -type, in which thermal X-ray emission from an optically thin plasma arises from the gas heated by colliding winds and/or collimated jets.

Typical X-ray luminosities of β -type symbiotics in the $0.3 - 2.4$ keV band that goes from 10^{30} to 10^{31} erg s^{-1} (Luna et al. 2013). The luminosities of 4XMM J184650.6–022907 in this energy band are $\sim 4.8 \times 10^{30}$ and $\sim 9.0 \times 10^{30}$ erg s^{-1} for Obs1 and Obs2, respectively, estimated with the best-fit model of Table 3 (right column). A striking characteristic of the X-ray emission from 4XMM J184650.6–022907 is its variability, namely the flux increases by factor ~ 2 between 2011 and 2018. A similar behavior has been observed in AG Peg, a β -type symbiotic stars that presented an outburst in 2015. This star has been extensively studied in the X-ray domain since its discover by ROSAT in 1993. It was observed with Swift in 2013 and 2015–2016, and with XMM-Newton in 2017. The X-ray emission, which was modeled by an optically thin plasma, increased by a factor 2 during the active phase in 2015, with respect to the pre- and post-outburst fluxes (Zhekov & Tomov 2018). While the X-ray emission in the pre-outburst period is likely produced by plasma heated in the colliding-wind region of the binary system, the dominant heating mechanism during the active phase is probably accretion of the wind from the cool star into the WD (Zhekov & Tomov 2016) or, alternatively, shocks from the interaction between material ejected during the outburst and the ejecta and/or circumbinary material (Ramsay et al. 2016).

Regarding the radio continuum emission towards symbiotic stars, seminal studies like Seaquist et al. (1993) found that most shell burning symbiotics detected with the Very Large Array (VLA) had radio flux densities on the order of mJy, consistent with free-free emission from the ionized wind of the red giant. On the other hand, Weston (2016), studying a sample of 11 non-burning symbiotics with radio continuum observations, found that about half of the sources have faint radio flux densities of about $10 \mu\text{m}$ or less. Taking this into account, we searched for possible radio counterpart for the binary star BD–02 4739 using the 3 GHz radio continuum Very Large Array Sky Survey (VLASS; Lacy et al. 2020). Although the high sensitivity ($\sim 100 \mu\text{Jy beam}^{-1}$) and the high resolution ($\sim 2''$) of the data, we did not find any evidence of radio continuum emission related to the source, which is consistent with a scenario of non-burning WD-symbiotic star.

Summarizing, our multiwavelength analysis strongly suggests that 4XMM J184650.6–022907 is related to the spectroscopic binary star BD–02 4739, which would be a non-burning β -type WD-symbiotic system with a sub-giant donor star. The increase of the X-ray flux detected in the 2018 XMM-Newton observation could be a consequence of an active phase transited by the system. As pointed out by Sokoloski et al. (2016), in a non shell burning symbiotic, the optical emission is dominated by the red giant. This supports our hypothesis of Sec. 3.4.1, where we consider that the fluxes used to fit the SED come from the donor star.

4.3. *Is BD-02 4739 responsible for the gamma-ray emission of 4FGL J1846.9-0227?*

Symbiotic stars have been confirmed as potential gamma-ray sources in the GeV band, when they experience a nova eruption event (Li et al. 2020; Franckowiak et al. 2018; Abdo et al. 2010). Novae are thermonuclear explosions on a WD surface fueled by mass accreted from a companion star. Symbiotic novae have an evolved companion (e.g. red giant) with a dense wind as opposed to a main-sequence companion for classical novae (Ackermann et al. 2014). Current physical models suggest that shocked expanding gas from the symbiotic nova shell interacts with the dense wind of the red giant, and that particles can be accelerated effectively to produce π^0 decay γ -rays from proton-proton interactions (Franckowiak et al. 2018). The first Fermi-LAT gamma-ray detection of a nova was made in the symbiotic-like nova V407 Cyg in 2010 (Abdo et al. 2010), followed by few other examples such as V1535 Sco, V1534 Sco, and V745 Sco.

We constructed a light curve of the GeV emission of 4FGL J1846.9-0227 using data from the Incremental Fermi LAT 4th Source Catalog (4FGL-DR3), spanning 12 years of data (August 2008 - August 2020) with 1-year bins (Fig. 16). For comparison, we also shown the light curves of novae V5668 Sgr (4FGL J1837.6-2904) and V1369 Cen (4FGL J1353.3-5910), where we have marked the date of the optical maximum. Franckowiak et al. (2018) show that gamma-ray peak of novae is concurrent with the optical maximum and lasts for some tens of days. Thus, we wonder if BD-02 4739 experienced a nova event.

Although the source experiences an increase in the gamma photon flux between August 2019 and August 2020, it is important to note that it presents a considerably continuous gamma emission along the years, which is not compatible with the fact that classical and symbiotic novae are only found to be GeV-emitters during the outbursts. In addition, we have not found any near-infrared/optical correspondence (VISTA, ASAS, ASAS-SN, Gaia databases) that shows a nova event. It is worth noting that based on the optical magnitude of BD-02 4739, it would be very difficult that the putative nova has been missed by both professional and amateur observatories. Moreover, by considering its nearby distance (0.5 kpc), a nova event, if not missed by Fermi, it would be extremely brighter in gamma-rays than what it is shown in Fig. 16 (upper panel); for instance see the RS Oph 2021 case at a distance of about 2.5 kpc (Cheung et al. 2022).

In conclusion, in spite of these interesting and new results about this binary system, we discard it as the responsible of the detected GeV emission in the region.

4.4. *What about MYSO MSX G30?*

From our analysis based on ALMA data, we found that the confirmed MYSO MSX G30 is associated with a dense molecular core, which presents evidence of star formation activity due to the presence of numerous molecular lines (Fig. 4), which are characteristic of hot molecular cores. This chemical richness is an interesting issue to be studied in deep in a future work. In particular, what is most relevant to this study is the detection of formaldehyde molecular outflows (see Fig. 5), which could explain the γ -ray emission of the Fermi-LAT source, as it was proposed by Munar-Adrover et al. (2011). However, based on the position of MYSO MSX G30 at the border of the confidence ellipse of the Fermi-LAT source, and the fact that the MYSO does not present any X-ray or centimeter radio emissions associated, we suggest that, it is very likely that the molecular outflows detected towards this MYSO are not energetic enough to be responsible for the gamma-ray emission. Therefore, we

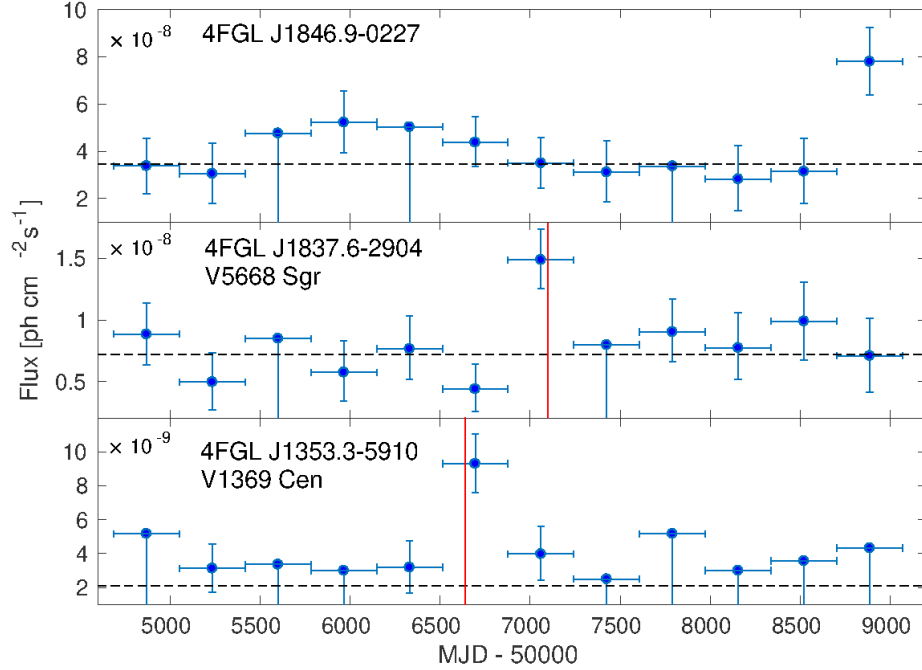


Figure 16. 12 years light curves of Fermi, for 4FGL J1846.9–0227 (top), V5668 Sgr (middle), and V1369 Cen (bottom). Each temporal bin corresponds to 1 year of data (starting August 2008). The horizontal dotted line is the time-averaged flux and the vertical red lines indicate the maximum of the optical novae. Fluxes with significance σ ($= \sqrt{TS}$) < 2 are shown as 95% confidence upper limits, where TS is the test statistics reported in the 4FGL-DR3 catalog for each epoch.

conclude that it is very unlikely that the counterpart of the high-energy source is such a young protostar.

4.5. What about IRAS 18443-0231?

The non-thermal nature of the radio continuum emission from IRAS 18443-0231 and the morphology of the continuum emission at 3 GHz indicate the presence of jets and accelerated particles. Additionally, we discovered a red-shifted molecular outflow supporting the presence of such jets in the region, which is in agreement with the detected H₂O maser (Urquhart et al. 2011).

Taking into account that this source is cataloged as a PN candidate, our findings indicate that IRAS 18443-0231 actually would be a proto-planet nebula (pPN), a short-lived transition (about 10^3 yr) from the asymptotic giant branch (AGB) to the PN phase. There are not much cases that non-thermal radio continuum emission was observed toward this kind of source (see the case of IRAS 15103-5754; Suárez et al. 2015), and on the other side, it is more common observing molecular outflows in pPNe (Cox et al. 2000; Lorenzo et al. 2021). The non-thermal radio emission in pPNe suggests that the emitting electrons arise at collisions between the fast and slow AGB winds that are observed predominantly on the front sides of the circumstellar shells (Bains et al. 2009).

Having discarded all the sources presented above as responsible of the gamma-ray emission, taking into account the location of IRAS 18443-0231 (almost at the center of the Fermi confidence ellipse), and mainly considering the presence of non-thermal jets accelerating particles, we wonder if IRAS 18443-0231 could be the counterpart of 4FGL J1846.9–0227.

As mention by Suárez et al. (2015) for IRAS 15103-5754, the radio spectral index $\alpha = -0.47 \pm 0.08$ measured in IRAS 18443-0231 is similar to that found in synchrotron emission in galaxies with active nuclei. Following the authors, in the energy conditions of PNe, mass-loss processes can produce collisionless, non-relativistic shocks, and electrons may undergo diffusive shock acceleration up to very high velocities ('first-order Fermi acceleration'). In such a scenario, in which particles are accelerated, and in addition the source seems to be embedded in dense molecular gas (see Sect. 3.5), processes such as proton-proton collisions and relativistic Bremsstrahlung are likely to occur generating gamma-rays. In that case, IRAS 18443-0231 would be the responsible of the gamma-ray emission. If this is the case, it would be the first reported pPN related to very high energy emission, and hence, multiwavelength dedicated observations and modeling are necessary to understand the mechanisms of gamma-rays production.

5. SUMMARY AND CONCLUDING REMARK

In previous works the nature of the Fermi-LAT source 4FGL J1846.9-0227 was discussed. In one of them it was suggested to be a blazar, and in other one it was mentioned the presence of a massive protostar within the Fermi confidence ellipse suggesting a possible association. Considering this discrepancy, in this work, we analyzed several counterpart candidates to the gamma-ray source based on a multiwavelength analysis.

First of all, from JVLA data we determined the thermal nature of a new extended radio source in the field, which indicates that this uncatalogued radio continuum source is an HII region and not a supernova remnant, ruling out that such a source is responsible for the gamma-ray emission. Using ALMA data, we confirmed that MSX6C G030.1981-00.1691 is a massive protostar with molecular outflow activity. However, since its peripheral location respect to the Fermi 95% confidence ellipse, and the lack of associated X-ray and centimeter radio continuum emissions, it is very unlikely that this massive protostar is responsible of the gamma-ray emission.

We found that sources SwXF4 J184651.6-022507 and SwXF4 J184650.7-022904, previously suggested to be blazars, do not meet the mid-IR color-color criteria for this kind of sources. Additionally, they lie almost at the galactic plane, which weakens the possibility of a blazar detection. Moreover, the second one is related to the 4XMM 184650.6-022907 source, and based on XMM-Newton data, we found that this X-ray source, which lies closer to the center of the Fermi 95% confidence ellipse, is clearly associated with the spectroscopic binary star BD-02 4739. The X-ray spectrum of 4XMM 184650.6-022907 was well fitted by an optically thin thermal plasma model with a relatively low X-ray luminosity of about 10^{30} erg s $^{-1}$. The soft thermal nature of the X-ray spectrum discards that 4XMM 184650.6-022907 is associated with a blazar. In fact, the X-ray spectrum is consistent with a white-dwarf (WD) symbiotic system. Thus, taking into account the results of the analysis of the X-ray data and the optical/infrared SED, we conclude that BD-02 4739 is a non-burning shell β -type WD symbiotic system with a sub-giant donor star. The way that this source can be considered as the responsible for the gamma emission is that it had experimented a nova event. Our findings discard such a possibility.

Finally, we found that IRAS 18443-0231, cataloged as a PN candidate located at a distance of about 8 kpc, is actually a protoplanetary nebula. IRAS 18443-0231 is the closest source in the region to the center of the Fermi 95% confidence ellipse. We discovered non-thermal radio continuum emission toward such a source (spectral index $\alpha = -0.47 \pm 0.08$), indicating syncrotron emission likely due to

particles accelerated in jets. Additionally, we discovered a molecular outflow, supporting the presence of jets, and we found that the source is embedded in a dense molecular clump. IRAS 18443-0231 presents hard X-ray extended emission, with the same inclination as the molecular outflow.

Considering all the presented results, we conclude that the most promising source to be associated with 4FGL J1846.9–0227 is IRAS 18443-0231. The detection of synchrotron emission indicate that particles are accelerated at high velocities in the region, and considering that source is embedded in a dense molecular clump, we suggest that processes such as proton-proton collisions and relativistic Bremsstrahlung are likely to occur. If this is the case, it would be the first reported protoplanetary nebula related to very high energy emission, and hence, multiwavelength dedicated observations and modeling are necessary to understand the mechanisms of gamma-rays production in this kind of source.

ACKNOWLEDGMENTS

M.O., A.P., and S.P. are members of the Carrera del Investigador Científico of CONICET, Argentina. This work was partially supported by the Argentina grants PIP 2021 11220200100012 and PICT 2021-GRF-TII-00061 awarded by CONICET and ANPCYT. This work is based on the following ALMA data: ADS/JAO.ALMA # 2015.1.01312. ALMA is a partnership of ESO (representing its member states), NSF (USA) and NINS (Japan), together with NRC (Canada), MOST and ASIAA (Taiwan), and KASI (Republic of Korea), in cooperation with the Republic of Chile. The Joint ALMA Observatory is operated by ESO, AUI/NRAO and NAOJ.

REFERENCES

Abdelfatah, A. S., Nasser, M. A., Abdelbar, A. M., & Beheary, M. M. 2021, *Journal of High Energy Astrophysics*, 31, 12, doi: [10.1016/j.jheap.2021.05.001](https://doi.org/10.1016/j.jheap.2021.05.001)

Abdo, A. A., Ackermann, M., Ajello, M., et al. 2010, *Science*, 329, 817, doi: [10.1126/science.1192537](https://doi.org/10.1126/science.1192537)

Abdollahi, S., Acero, F., Baldini, L., et al. 2022, *ApJS*, 260, 53, doi: [10.3847/1538-4365/ac6751](https://doi.org/10.3847/1538-4365/ac6751)

Acero, F., Ackermann, M., Ajello, M., et al. 2013, *ApJ*, 773, 77, doi: [10.1088/0004-637X/773/1/77](https://doi.org/10.1088/0004-637X/773/1/77)

Ackermann, M., Ajello, M., Albert, A., et al. 2014, *Science*, 345, 554, doi: [10.1126/science.1253947](https://doi.org/10.1126/science.1253947)

Anderson, L. D., Armentrout, W. P., Johnstone, B. M., et al. 2015, *ApJS*, 221, 26, doi: [10.1088/0067-0049/221/2/26](https://doi.org/10.1088/0067-0049/221/2/26)

Anderson, L. D., & Bania, T. M. 2009, *ApJ*, 690, 706, doi: [10.1088/0004-637X/690/1/706](https://doi.org/10.1088/0004-637X/690/1/706)

Anderson, L. D., Bania, T. M., Balser, D. S., & Rood, R. T. 2011, *ApJS*, 194, 32, doi: [10.1088/0067-0049/194/2/32](https://doi.org/10.1088/0067-0049/194/2/32)

Araudo, A. T., & Rodríguez, L. F. 2012, in American Institute of Physics Conference Series, Vol. 1505, *High Energy Gamma-Ray Astronomy: 5th International Meeting on High Energy Gamma-Ray Astronomy*, ed. F. A. Aharonian, W. Hofmann, & F. M. Rieger (AIP), 281–284, doi: [10.1063/1.4772252](https://doi.org/10.1063/1.4772252)

Bahramian, A., & Degenaar, N. 2023, in *Handbook of X-ray and Gamma-ray Astrophysics*. Edited by Cosimo Bambi and Andrea Santangelo, 120, doi: [10.1007/978-981-16-4544-0_94-1](https://doi.org/10.1007/978-981-16-4544-0_94-1)

Bains, I., Cohen, M., Chapman, J. M., Deacon, R. M., & Redman, M. P. 2009, *MNRAS*, 397, 1386, doi: [10.1111/j.1365-2966.2009.14845.x](https://doi.org/10.1111/j.1365-2966.2009.14845.x)

Ballet, J., Bruel, P., Burnett, T. H., Lott, B., & The Fermi-LAT collaboration. 2023, arXiv e-prints, arXiv:2307.12546, doi: [10.48550/arXiv.2307.12546](https://doi.org/10.48550/arXiv.2307.12546)

Blackman, E. G., Frank, A., Markiel, J. A., Thomas, J. H., & Van Horn, H. M. 2001, *Nature*, 409, 485, doi: [10.1038/35054008](https://doi.org/10.1038/35054008)

Boboltz, D. A., & Marvel, K. B. 2005, *ApJL*, 627, L45, doi: [10.1086/431931](https://doi.org/10.1086/431931)

Bosch-Ramon, V., Romero, G. E., Araudo, A. T., & Paredes, J. M. 2010, *A&A*, 511, A8, doi: [10.1051/0004-6361/200913488](https://doi.org/10.1051/0004-6361/200913488)

Brunthaler, A., Menten, K. M., Dzib, S. A., et al. 2021, *A&A*, 651, A85, doi: [10.1051/0004-6361/202039856](https://doi.org/10.1051/0004-6361/202039856)

Busch, L. A., Belloche, A., Garrod, R. T., Müller, H. S. P., & Menten, K. M. 2022, *A&A*, 665, A96, doi: [10.1051/0004-6361/202243383](https://doi.org/10.1051/0004-6361/202243383)

Cao, Z., Chen, S., Liu, R., & Yang, R. 2023, *Annual Review of Nuclear and Particle Science*, 73, 341, doi: [10.1146/annurev-nucl-112822-025357](https://doi.org/10.1146/annurev-nucl-112822-025357)

Carey, S. J., Noriega-Crespo, A., Price, S. D., et al. 2005, in *American Astronomical Society Meeting Abstracts*, Vol. 207, *American Astronomical Society Meeting Abstracts*, 63.33

Cheung, C. C., Johnson, T. J., Jean, P., et al. 2022, *ApJ*, 935, 44, doi: [10.3847/1538-4357/ac7eb7](https://doi.org/10.3847/1538-4357/ac7eb7)

Churchwell, E., Babler, B. L., Meade, M. R., et al. 2009, *PASP*, 121, 213, doi: [10.1086/597811](https://doi.org/10.1086/597811)

Cox, P., Lucas, R., Huggins, P. J., et al. 2000, *A&A*, 353, L25

Cutri, R. M., Wright, E. L., Conrow, T., et al. 2021, *VizieR Online Data Catalog: AllWISE Data Release (Cutri+ 2013)*, *VizieR On-line Data Catalog: II/328*. Originally published in: *IPAC/Caltech* (2013)

Cyganowski, C. J., Whitney, B. A., Holden, E., et al. 2008, *AJ*, 136, 2391, doi: [10.1088/0004-6256/136/6/2391](https://doi.org/10.1088/0004-6256/136/6/2391)

D'Abrusco, R., Massaro, F., Ajello, M., et al. 2012, *ApJ*, 748, 68, doi: [10.1088/0004-637X/748/1/68](https://doi.org/10.1088/0004-637X/748/1/68)

de Jager, C., & Nieuwenhuijzen, H. 1987, *A&A*, 177, 217

de Oña Wilhelmi, E., López-Coto, R., & Su, Y. 2023, *MNRAS*, 523, 105, doi: [10.1093/mnras/stad1413](https://doi.org/10.1093/mnras/stad1413)

Di Francesco, J. 2008, in *American Astronomical Society Meeting Abstracts*, Vol. 212, *American Astronomical Society Meeting Abstracts #212*, 96.03

Dokara, R., Brunthaler, A., Menten, K. M., et al. 2021, *A&A*, 651, A86, doi: [10.1051/0004-6361/202039873](https://doi.org/10.1051/0004-6361/202039873)

Fan, H., Nakashima, J.-i., Engels, D., et al. 2024, *ApJS*, 270, 13, doi: [10.3847/1538-4365/ad0458](https://doi.org/10.3847/1538-4365/ad0458)

Fornasini, F. M., Antoniou, V., & Dubus, G. 2023, *arXiv e-prints*, arXiv:2308.02645, doi: [10.48550/arXiv.2308.02645](https://doi.org/10.48550/arXiv.2308.02645)

Franckowiak, A., Jean, P., Wood, M., Cheung, C. C., & Buson, S. 2018, *A&A*, 609, A120, doi: [10.1051/0004-6361/201731516](https://doi.org/10.1051/0004-6361/201731516)

Gaia Collaboration. 2022, *VizieR Online Data Catalog*, I/357

Haberl, F., Maitra, C., Vasilopoulos, G., et al. 2022, *A&A*, 662, A22, doi: [10.1051/0004-6361/202243301](https://doi.org/10.1051/0004-6361/202243301)

Hasinger, G., & van der Klis, M. 1989, *A&A*, 225, 79

Helfand, D. J., Becker, R. H., White, R. L., Fallon, A., & Tuttle, S. 2006, *AJ*, 131, 2525, doi: [10.1086/503253](https://doi.org/10.1086/503253)

Honma, M., Oyama, T., Hachisuka, K., et al. 2000, *PASJ*, 52, 631, doi: [10.1093/pasj/52.4.631](https://doi.org/10.1093/pasj/52.4.631)

Irabor, T., Hoare, M. G., Oudmaijer, R. D., et al. 2018, *MNRAS*, 480, 2423, doi: [10.1093/mnras/sty1929](https://doi.org/10.1093/mnras/sty1929)

Kaur, A., Falcone, A. D., Stroh, M. D., Kennea, J. A., & Ferrara, E. C. 2019, *ApJ*, 887, 18, doi: [10.3847/1538-4357/ab4ceb](https://doi.org/10.3847/1538-4357/ab4ceb)

Kerby, S., Kaur, A., Falcone, A. D., et al. 2021, *ApJ*, 923, 75, doi: [10.3847/1538-4357/ac2e91](https://doi.org/10.3847/1538-4357/ac2e91)

Kretschmar, P., Fürst, F., Sidoli, L., et al. 2019, *NewAR*, 86, 101546, doi: [10.1016/j.newar.2020.101546](https://doi.org/10.1016/j.newar.2020.101546)

Lacy, M., Baum, S. A., Chandler, C. J., et al. 2020, *PASP*, 132, 035001, doi: [10.1088/1538-3873/ab63eb](https://doi.org/10.1088/1538-3873/ab63eb)

Li, K.-L., Hamsch, F.-J., Munari, U., et al. 2020, *ApJ*, 905, 114, doi: [10.3847/1538-4357/abc3be](https://doi.org/10.3847/1538-4357/abc3be)

Lin, D., Remillard, R. A., & Homan, J. 2009, *ApJ*, 696, 1257, doi: [10.1088/0004-637X/696/2/1257](https://doi.org/10.1088/0004-637X/696/2/1257)

Liu, Q. Z., van Paradijs, J., & van den Heuvel, E. P. J. 2006, *A&A*, 455, 1165, doi: [10.1051/0004-6361:20064987](https://doi.org/10.1051/0004-6361:20064987)

Lorenzo, M., Teyssier, D., Bujarrabal, V., et al. 2021, *A&A*, 649, A164, doi: [10.1051/0004-6361/202039592](https://doi.org/10.1051/0004-6361/202039592)

Lumsden, S. L., Hoare, M. G., Urquhart, J. S., et al. 2013, *ApJS*, 208, 11, doi: [10.1088/0067-0049/208/1/11](https://doi.org/10.1088/0067-0049/208/1/11)

Luna, G. J. M., Sokoloski, J. L., Mukai, K., & Nelson, T. 2013, *A&A*, 559, A6, doi: [10.1051/0004-6361/201220792](https://doi.org/10.1051/0004-6361/201220792)

Madejski, G. G., & Sikora, M. 2016, *ARA&A*, 54, 725, doi: [10.1146/annurev-astro-081913-040044](https://doi.org/10.1146/annurev-astro-081913-040044)

Mitsuda, K., Inoue, H., Nakamura, N., & Tanaka, Y. 1989, PASJ, 41, 97

Muerset, U., Wolff, B., & Jordan, S. 1997, A&A, 319, 201

Munar-Adrover, P., Paredes, J. M., & Romero, G. E. 2011, A&A, 530, A72, doi: [10.1051/0004-6361/201116580](https://doi.org/10.1051/0004-6361/201116580)

Okoda, Y., Oya, Y., Sakai, N., Watanabe, Y., & Yamamoto, S. 2020, ApJ, 900, 40, doi: [10.3847/1538-4357/aba51e](https://doi.org/10.3847/1538-4357/aba51e)

Purcell, C. R., Hoare, M. G., & Diamond, P. 2008, in Astronomical Society of the Pacific Conference Series, Vol. 387, Massive Star Formation: Observations Confront Theory, ed. H. Beuther, H. Linz, & T. Henning, 389

Ramsay, G., Sokoloski, J. L., Luna, G. J. M., & Nuñez, N. E. 2016, MNRAS, 461, 3599, doi: [10.1093/mnras/stw1546](https://doi.org/10.1093/mnras/stw1546)

Rangelov, B., Yang, H., Williams, B., et al. 2024, ApJ, 961, 26, doi: [10.3847/1538-4357/ad09da](https://doi.org/10.3847/1538-4357/ad09da)

Reich, W., Reich, P., & Fuerst, E. 1990, A&AS, 83, 539

Rigby, A. J., Moore, T. J. T., Plume, R., et al. 2016, MNRAS, 456, 2885, doi: [10.1093/mnras/stv2808](https://doi.org/10.1093/mnras/stv2808)

Rodrigo, C., & Solano, E. 2020, in XIV.0 Scientific Meeting (virtual) of the Spanish Astronomical Society, 182

Sahai, R., Kastner, J. H., Frank, A., Morris, M., & Blackman, E. G. 2003, ApJL, 599, L87, doi: [10.1086/381316](https://doi.org/10.1086/381316)

Seaquist, E. R., Krogulec, M., & Taylor, A. R. 1993, ApJ, 410, 260, doi: [10.1086/172742](https://doi.org/10.1086/172742)

Sidoli, L., & Paizis, A. 2018, MNRAS, 481, 2779, doi: [10.1093/mnras/sty2428](https://doi.org/10.1093/mnras/sty2428)

Smith, N. 2014, ARA&A, 52, 487, doi: [10.1146/annurev-astro-081913-040025](https://doi.org/10.1146/annurev-astro-081913-040025)

Sokoloski, J., Lawrence, S., Crotts, A. P. S., & Mukai, K. 2016, in Accretion Processes in Cosmic Sources, 21, doi: [10.22323/1.288.0021](https://doi.org/10.22323/1.288.0021)

Suárez, O., Gómez, J. F., Bendjoya, P., et al. 2015, ApJ, 806, 105, doi: [10.1088/0004-637X/806/1/105](https://doi.org/10.1088/0004-637X/806/1/105)

Tychoniec, L., van Dishoeck, E. F., van't Hoff, M. L. R., et al. 2021, A&A, 655, A65, doi: [10.1051/0004-6361/202140692](https://doi.org/10.1051/0004-6361/202140692)

Urquhart, J. S., Morgan, L. K., Figura, C. C., et al. 2011, MNRAS, 418, 1689, doi: [10.1111/j.1365-2966.2011.19594.x](https://doi.org/10.1111/j.1365-2966.2011.19594.x)

van der Meer, A., Kaper, L., di Salvo, T., et al. 2005, A&A, 432, 999, doi: [10.1051/0004-6361:20041288](https://doi.org/10.1051/0004-6361:20041288)

Weston, J. H. S. 2016, PhD thesis, Columbia University, New York

Yang, A. Y., Thompson, M. A., Urquhart, J. S., & Tian, W. W. 2018, ApJS, 235, 3, doi: [10.3847/1538-4365/aaa297](https://doi.org/10.3847/1538-4365/aaa297)

Yang, A. Y., Tian, W. W., Zhu, H., Leahy, D. A., & Wu, D. 2016, ApJS, 223, 6, doi: [10.3847/0067-0049/223/1/6](https://doi.org/10.3847/0067-0049/223/1/6)

Zhekov, S. A., & Tomov, T. 2016, MNRAS, 461, 286, doi: [10.1093/mnras/stw1339](https://doi.org/10.1093/mnras/stw1339)

Zhekov, S. A., & Tomov, T. V. 2018, MNRAS, 481, 5156, doi: [10.1093/mnras/sty2644](https://doi.org/10.1093/mnras/sty2644)